UNIVERSITY OF THESSALY

POLYTECHNIC SCHOOL

DEPARTMENT OF MECHANICAL ENGINEERING

LABORATORY OF MATERIALS

Diploma Thesis

Study of the microstructure and the mechanical properties of the aerospace aluminum alloy 2024 using the computational software TC-PRISMA

By

Zisopoulos Ioannis

Supervisor:

Dr. Helen Kamoutsi

Submitted for the Partial Fulfillment of the requirements for

the degree of Diploma in Mechanical Engineering

Certified by the members of the Thesis Committee:

First Examiner (Supervisor) — Dr. Helen Kamoutsi
Lab Teaching Staff
Department of Mechanical Engineering
University of Thessaly

Second Examiner — Dr. Gregory. N. Haidemenopoulos
Professor of Physical Metallurgy
Department of Mechanical Engineering
University of Thessaly

Third Examiner — Dr. Alexis Kermanidis
Professor of Mechanical Behavior of Materials
Department of Mechanical Engineering
University of Thessaly

Table of Contents

Chapter 1 Introduction 11
Chapter 2 Literature Review 13
2.1 Material Studied 13
2.2 Heat Treatment of AA2XXX 13
2.2.1 Solution Heat Treatment 13
2.2.2 Quenching 13
2.2.3 Ageing 14
2.3 Kinetics of the Precipitation 15
2.3.1 Nucleation 15
2.3.2 Vacancies and PFZs 19
2.3.3 Growth 20
2.3.4 Precipitation Kinetics 21
2.3.5 Coarsening 24
2.4 Precipitation Strengthening Mechanisms 26
2.5 Other Strengthening Mechanisms 28
2.5.1 Cluster Hardening 28
2.5.2 Chemical Hardening 29
2.6 Precipitation in 2xxx series of Aluminum Alloys 29
2.6.1 Precipitation Sequence in 2xxx series of Aluminum Alloys 29
2.6.2 Alloying Elements 31
Chapter 3 Methodology 33
3.1 Material Studied 33
3.2 Heat Treatment and Microhardness Values 33
3.3 Modeling Precipitation with KW numerical method 33
3.3.1 KW Methodology 33
3.3.2 Utilizing TC-PRISMA module to simulate aging in the experiment 35
Chapter 4 Results 37
4.1 Microhardness Measurements 37
4.2 Hardness evolution for different compositions 43
4.2.1 Model based on S-phase spherical precipitates 43
4.2.2 Model based on S'-phase, S-phase and needle morphology precipitates 50
Chapter 5 Conclusions 59
Chapter 6 References 61

Table of Figures

Figure 2-1: The change in free energy of the newly formed phase in relation to the particle radius during the process of nucleation. 16
Figure 2-2: The correlation between the change in free energy and the size of particles, considering both coherent and semicoherent particles [9]. 17
Figure 2-3. Coherency loss mechanisms. (a) Dislocation punching from interface. (b) Capture of matrix dislocation. (c) Nucleation at edge of plate repeated as plate lengthens. (d) Loop expansion by vacancy condensation in the precipitate [13]. 18
Figure 2-4: (a) Phase Diagram, (b) free energy at $T_{0,}$ (c) concentration profile [13]. 21
Figure 2-5: The rate of diffusional transformation as a function of temperature [9]. 21
Figure 2-6: (a) IT (isothermal transformation) diagram, (b) Fraction function for three different temperatures 22
Figure 2-7: An S-curve consisting of 1: induction period, 2: growth period and 3: impingement period [9]. 23
Figure 2-8: (a) Free energy and the concentration of the α and β phases, considering different values of the curvature radius of the β phase particles, (b) B atoms diffuse from smaller to bigger particles [9]. 25
Figure 2-9: The relationship between coarsening rates and radius for two distinct mean radius values, as described by the Greenwood [9]. 26
Figure 2-10: Orowan mechanism 28
Figure 2-11: The enhancement of strength due to the presence of penetrable and impenetrable particles, considering the size of the particles or the aging time. 28
Figure 4-1: Changes in microhardness as a function of aging time during an aging process at 150°C [56]. 37
Figure 4-2: Changes in microhardness over time during an aging process at 150°C, for different mobility prefactors [56]. 38
Figure 4-3: Changes in microhardness as a function of aging time during an aging process at 160°C [56]. 38
Figure 4-4: Changes in microhardness over time during an aging process at 160°C, for different mobility prefactors [56]. 39
Figure 4-5: Changes in microhardness as a function of aging time during an aging process at 170°C [57]. 40
Figure 4-6: Changes in microhardness over time during an aging process at 170°C, for different mobility prefactors [57]. 40
Figure 4-7: Changes in microhardness as a function of aging time during an aging process at 170°C [58]. 41
Figure 4-8: Changes in microhardness over time during an aging process at 170°C, for different mobility prefactors [58]. 41
Figure 4-9: Changes in microhardness as a function of aging time during an aging process at 210°C [58]. 42

Figure 4-10: Changes in microhardness over time during an aging process at 210°C, for different mobility prefactors [58]..... 43
Figure 4-11: Hardness evolution as a function of aging time across different copper concentrations compared to Floratos's experiment, at 170°C [57]..... 44
Figure 4-12: Hardness evolution as a function of aging time across different copper concentrations compared to Karantonidis's experiment, at 170°C [58]..... 44
Figure 4-13: Hardness evolution as a function of aging time across different magnesium concentrations compared to Floratos's experiment, at 170°C [57]..... 45
Figure 4-14: Hardness evolution as a function of aging time across different magnesium concentrations compared to Karantonidis's experiment, at 170°C [58]..... 46
Figure 4-15: Various alloy compositions, with the alloy Al-4.4Cu-1.5Mg with a mobility prefactor of 0.1 being the best approximation to Floratos's findings at 170°C..... 47
Figure 4-16: Various alloy compositions, with the alloy Al-4.35Cu-1.5Mg with a mobility prefactor of 0.6 being the best approximation to Karantonidis's findings at 170°C..... 47
Figure 4-17 Hardness evolution as a function of aging time across different copper concentrations compared to Karantonidis's experiment, at 210°C [58]..... 48
Figure 4-18: Hardness evolution as a function of aging time across different magnesium concentrations compared to Karantonidis's experiment, at 210°C [58]..... 49
Figure 4-19: Various alloy compositions, with the alloy Al-4.35Cu-1.5Mg with a mobility prefactor of 0.3 being the best approximation to Karantonidis's findings at 210°C..... 49
Figure 4-20: Hardness evolution of S-Prime and S-Phase in default settings and needle morphology, in 170°C. 50
Figure 4-21: Changes in microhardness as a function of time during an aging process at 170°C for needle shaped precipitates compared to Floratos's experiment. 51
Figure 4-22: Changes in microhardness as a function of time during an aging process at 170°C for needle shaped precipitates compared to Karantonidis's experiment. 51
Figure 4-23: Changes in microhardness as a function of time during an aging process at 210°C for needle shaped precipitates compared to Karantonidis's experiment. 52
Figure 4-24: Nucleation rates for different mobility prefactors for the Al-4.35Cu-1.5Mg alloy, at 170°C. 53
Figure 4-25: Nucleation rates for different mobility prefactors for the Al-4.35Cu-1.5Mg alloy, at 210°C. 53
Figure 4-26: Evolution of number density and nucleation rate in the aging process of 210°C, in the Al-4.35Cu-1.5Mg alloy with a mobility prefactor of 0.1. 54
Figure 4-27: Evolution of number density and nucleation rate in the aging process of 170°C, in the Al-4.35Cu-1.5Mg alloy with a mobility prefactor of 0.2. 54
Figure 4-28: Evolution of the normalized driving force during aging at 170°C and 210°C. 55
Figure 4-29: Evolution of number density and volume fraction in the aging process of 170°C, in the Al-4.35Cu-1.5Mg alloy with a mobility prefactor of 0.2. 56
Figure 4-30: Evolution of number density and volume fraction in the aging process of 210°C, in the Al-4.35Cu-1.5Mg alloy with a mobility prefactor of 0.1. 56
Figure 4-31: Radius and length size distributions of the S phase precipitates, at peak hardness in 170°C , for the Al-4.35Cu-1.5Mg alloy with needle-shaped precipitates (A.R:10) and a mobility prefactor of 0.2..... 57

Figure 4-32: Radius and length size distributions of the S phase precipitates, at peak hardness in 210°C , for the Al-4.35Cu-1.5Mg alloy with needle-shaped precipitates (A.R:10) and a mobility prefactor of 0.1. 57
Figure 4-33: Precipitate Composition (% w/w) during aging for both 170°C and 210°C, for the Al-4.35Cu-1.5Mg alloy with needle-shaped precipitates (A.R:10) and a mobility prefactor 0.2 and 0.1, respectively. 58

Table of Tables

Table 2-1: The arrangement of nucleation sites in descending order based on the decreasing activation energy for nucleation, from highest to lowest[13]. 19
Table 2-2: Different values of n-exponent in the JMAK equation [9,18]. 24

Acknowledgements

This undertaking was successfully carried out as part of the partial fulfillment of the criteria for the attainment of a Diploma in Mechanical Engineering at the University of Thessaly.

I would like to extend my heartfelt gratitude to Dr. Helen Kamoutsi, my supervisor, whose unwavering assistance was indispensable in achieving the objectives of this project.

Additionally, I wish to convey my special appreciation to Professor Gregory N Haidemenopoulos and Professor Alexis Kermanidis for graciously agreeing to participate as members of the three-person evaluation committee for my Diploma Thesis.

I would also like to convey my appreciation to my entire family, with a special mention to my parents, Sofia and Konstantinos, and my brothers, Prodromos and Panagiotis, for their unwavering support throughout my academic journey.

Abstract

The aluminum alloy AA2024 is a lightweight heat treatable alloy with multiple applications in aerospace and military aerospace structures. This particular alloy is classified within the 2xxx series of wrought aluminum alloys, commonly recognized as aircraft alloys, or Al-Cu-Mg alloys. Copper serves as the principal alloying element in this category, imparting notable strength while marginally compromising corrosion resistance. Historically labeled as duralumin, these alloys represent some of the earliest aluminum alloy formulations. Notably, alloy 2024 stands out as one of the most renowned and extensively employed alloys within the aviation sector. The unpropitious conditions that 2xxx alloys are summoned to deal, require very strict limits in properties like the resistance to stress corrosion cracking, high strength, and light weight. Aging-induced strengthening stands as the predominant and highly effective method for enhancing the hardness of these alloy series. The central mechanism behind strengthening in these alloys involves the formation of Mg-Cu clusters and, later, the incoherent and equilibrium S phase. Despite the numerous investigations conducted on microstructural changes during aging precipitation in Al-Cu-Mg alloys, certain aspects continue to evoke debates. In recent decades, computational modeling of aging precipitation using diverse simulation software has also garnered research attention. Motivated by the stringent demands and scientific curiosity surrounding Al-Cu-Mg alloys, the current thesis aims to explore microstructural transformations that occur during aging precipitation and establish their correlation with hardness evolution throughout the aging process. The research encompasses a comprehensive literature review, followed by practical methodologies such as microhardness assessments. Additionally, an aging treatment is simulated using the TC-PRISMA precipitation module, contributing to the investigative scope of this study.

Chapter 1 Introduction

The aluminum alloy 2024, belonging to the 2xxx series, shares the lightweight and heat-treatable characteristics characteristic of its alloy family, making it a versatile choice for various applications in aerospace structures. Its remarkable attributes, including resistance to stress corrosion cracking, are primarily attributed to tailored heat treatments. Typical constituents of 2xxx series alloys encompass copper and magnesium, occasionally complemented by smaller element additions (less than 0.6%), such as manganese, titanium, silicon, and chromium. A pivotal technique for fortifying these alloys involves aging heat treatment. The meticulous preparatory processes undertaken in these alloys hold vital significance to ensure that their properties align with stringent benchmarks mandated by the demanding conditions of their diverse applications, notably within the aerospace and military aerospace sectors.

Aging confers strength to the material through a precipitation mechanism, which entails the formation of finely dispersed precipitates that hinder the movement of dislocations. Preceding the aging heat treatment, a preliminary step involving solution treatment followed by rapid cooling is necessary. The primary goal of the solution treatment is to expand the solubility limits of alloy constituents, thereby promoting the creation of a uniform solid solution through isothermal heating near eutectic temperatures. Swift cooling during quenching generates a supersaturated solid solution, setting the stage for subsequent precipitation. Aging procedures can be categorized as natural (occurring at room temperature) or artificial (involving intermediate temperatures). Natural aging leads to precipitation driven solely by supersaturation, while artificial aging leverages accelerated diffusion rates to facilitate precipitation.

Precipitation initiation initiates through nucleation of particles, typically occurring at specific sites such as each atom within the matrix for uniform nucleation, or defects in the structure for heterogeneous nucleation. The initial preference for nucleation rests with coherent metastable phases, as opposed to incoherent equilibrium phases, owing to the lower interfacial energy of the former. However, over time, the system inclines toward relinquishing the coherence between precipitates and the matrix due to the considerable strain energy inherent in a coherent interface. This shift from coherence to semi-coherence and, eventually, incoherence marks the progression. This transformation introduces distinct transitional sequences unique to each alloy type. Following nucleation, precipitate growth commences, driven by the diffusion of solute atoms from the matrix towards the precipitates. The growth process concludes when the composition of the new phase aligns with equilibrium conditions as dictated by the corresponding phase diagram. Despite seemingly achieving equilibrium, the system retains elevated interfacial energy, rendering it metastable in practice. Consequently, the system initiates a coarsening process to reduce its free energy. This process results in a decrease in precipitate density and an enlargement of precipitate size, leading to a coarser distribution incapable of effectively impeding dislocation glide. Thus, coarsening represents an undesired phenomenon in the context of precipitation strengthening.

Despite the extensive array of studies delving into microstructural attributes associated with precipitation in aluminum alloys of the 2xxx series—such as the nature of precipitate phases and the kinetics governing their transformations—certain aspects continue to elicit debate within the scientific community. Nonetheless, within the realm of aluminum alloys belonging to the 2xxx series, a widely acknowledged transition sequence prevails:

$$SSSS \rightarrow \text{GPB zones/Cu} - \text{Mg clusters/S}'' \rightarrow S'(metastable\ phase) \rightarrow S\ (equilibrium\ Al_2CuMg\ phase)$$

GPB zones, or Guinier Preston zones, manifest as clusters of precipitates observed in various aluminum alloy types, often representing the initial coherent precipitate phase. The metastable S' phase, preceding the equilibrium S phase, which holds prominence as the primary strengthening agent within this alloy series, are referred in the bibliography as being non distinguishable . However, certain studies extend the classification of main hardening phases for 2xxx series alloys to encompass Cu-Mg clusters as well, as the first hardening phase.

Over the past few decades, there has been a significant focus on anticipating the behavior of microstructures during aging precipitation. The impetus behind these inquiries is the potential utility of accurately simulating the precipitation process, which could provide valuable insights for digital alloy and process design. Among the numerical models that have demonstrated reliable outcomes, the Kampmann-Wagner-Numerical (KWN) model has garnered attention. This model, an extension of the Langer-Schwartz (LS) theory, posits that the particle size distribution (PSD) serves as a representation of the progression of precipitation. To tackle the intricacies of this challenge, the KWN approach discretizes the PSD and subsequently solves it directly.

Driven by both scientific curiosity and industrial significance attributed to the 2xxx alloys, this research endeavor seeks to enhance our comprehension of the aging precipitation phenomena within the microstructure. The study aims to establish correlations between these phenomena and the concurrent evolution of hardness during the aging process. Additionally, this study aims to investigate the response of the AA2024 alloy when subjected to diverse aging treatments. In pursuit of these goals, the AA2024 alloy under investigation, underwent an effort to simulate various aging treatments using the TC-PRISMA precipitation module while microhardness assessments from previous researchers were used to compare the results.

Thesis Outline:

Chapter 1 - Introduction

Chapter 2 - Literature Review

Chapter 3 - Methodology

Chapter 4 - Results

Chapter 5 - Conclusions

Chapter 2 Literature Review

2.1 Material Studied

Aluminum alloys have become increasingly popular in the aviation and aerospace industries due to their excellent mechanical properties such as high strength to weight ratio, good plasticity, formability, fracture toughness, and fatigue resistance.[1–7] The 2xxx series, which includes AA2024, is particularly widely used and constitutes over 40% of the materials utilized in the aircraft industry [5]. AA2024 is a precipitation-hardened alloy that derives its mechanical properties from an appropriate heat treatment that involves homogenization at around 500°C, followed by quenching and ageing at various temperatures ranging from room temperature to 210°C [6]. Copper and magnesium are the main alloying elements in these alloys along with minor additions of other elements such as zinc, iron, manganese and titanium [3,8].

2.2 Heat Treatment of AA2XXX

The process of heat treatment is a crucial technique for improving the strength of various types of alloys, including those made of aluminum, and it is widely implemented for this purpose. This process involves three sequential operations. Solution heat treatment is the first one and its aim is the aluminum alloy to be heated isothermally to a specific temperature range above the solvus line in the phase diagram. The objective of the aforementioned procedure is to dissolve any casting precipitates and distribute the alloying elements uniformly throughout the aluminum matrix. Subsequently, the aluminum alloy is quenched, which rapidly cools the material, to prevent any new precipitates from forming. Therefore, the process results in a supersaturated solid solution (SSSS), leading to a significant driving force for precipitation. The last operation that takes place is aging. Through aging, the alloy is reheated to a medium temperature, typically 150°C - 200°C, to allow for precipitation hardening. The latter mechanism is the one that gives the final material its improved mechanical properties[9,10].

2.2.1 Solution Heat Treatment

The main objective of this process, as previously mentioned, is the achievement of a uniform microstructure that is composed of a single phase and is conducted for the dissolution of any large precipitates that may exist in the material following the casting process. These particles harm the desired mechanical properties of the alloy. To dissolve the precipitates without causing the metal to melt, the solution treatment process requires heating the aluminum to a temperature that is high enough. As temperature increases, so does the solid solubility of the alloying elements and the dissolution rate of the unwanted precipitates. As it can be understood, this procedure has to take place in a very strict temperature range in order to ensure the required characteristics. For the aluminium alloys in this thesis, this range is within 450 °C to 600 °C and depends on a large extent of how the alloying elements have an impact on the solid solubility and the eutectic melting points of the system. Another important key component is the duration of this isothermal holding and varies depending on the size[9–12].

2.2.2 Quenching

As mentioned before, when the alloy has been treated isothermally, the following procedure is quenching. During this process, the material is cooled rapidly by submerging it in cold water and this way precipitation is obstructed. However, if the geometry of the specimen is complex, quenching occurs at slower rates, in water at higher temperatures, in order to eliminate stress that might build internally. The purpose of this procedure is to in fact ‘freeze’ the uniform microstructure achieved earlier by not allowing any precipitation phenomena to take place. Slower rates allow these

phenomena to occur, so the desired strength will not reach its maximum potential value. Under those circumstances, the particles that formed by slow cooling can not hinder the movement of the dislocations, because of their size, while concurrently they consume solute from the matrix and thus reducing the hardening precipitates that could have been formed. Once quenching is complete, the aluminum attains a ductile state, which is the optimal condition for shaping the metal into its final form as the end-product [9–11].

2.2.3 Ageing

The third, and final, treatment is thermal ageing. The homogeneous microstructure that has been retained prior to this process generate a driving force for precipitation leading to the formation of small and stable particles that act as barriers to the movement of dislocations, hence increasing substantially the yield strength and the hardness of the alloy. There are two types of ageing: natural and artificial. Natural ageing takes place at room temperature and the driving force is the supersaturation of the matrix. It is generally a very slow progress for the reason that peak strength is achieved after months. On the other hand, artificial ageing occurs at an increased temperature taking advantage of the higher diffusional rates and, thus leading to higher strength in a lot less time [10].

During thermal ageing, the material sustains microstructural changes over the course of time, leading to alterations in its mechanical properties. For the 2000 series aluminium alloys, the sequence of transformations is:

supersaturated solid solution → GP zones →intermediate precipitates → equilibrium precipitates

GP zones or Guinier-Preston Zones is the first precipitate that forms during ageing in 2000 series. These zones are coherent clusters of solute atoms, that are mainly copper, dispersed within the aluminum matrix. As aging progresses, intermediate precipitates that are either coherent or semicoherent nucleate homogeneously on GP zones or heterogeneously at the grain boundaries. After nucleation is complete, growth of the precipitates follows, and the mechanical properties are improved. Finally, the metastable precipitates turn into equilibrium precipitates and the strength gains are maximized. Excessive heat treatment at high temperatures and for extended periods of time, which is called over-aging, activates the coarsening regime. During coarsening, equilibrium precipitates continue to grow in size at the expense of the smaller ones which inevitably leads to degradation of the strength and hardness of the material. All these transformations and mechanisms that are mentioned above will be analyzed to a greater extent.

2.3 Kinetics of the Precipitation

Precipitation refers to a thermally driven diffusional transformation process. This process involves the creation of both stable and metastable phases through the mechanisms of nucleation and growth. The initiation of a new phase occurs when there is a significant local change in composition. Once formed, these nuclei develop into precipitates as solute diffuses from the surrounding matrix towards them.

2.3.1 Nucleation

The chemical force that induces the formation of precipitates, as mentioned earlier, relies on the degree of supersaturation that is achieved after the quenching. If we assume a dilute solution, the chemical driving force can be expressed as follows:

$$\Delta G_V = -\frac{RT}{V_m} ln\frac{c_0}{c} \quad 2\text{-}1$$

Where R is the universal gas constant, V_m is the molar volume of the precipitate, c_0 is the composition of the alloy, c is the composition of the supersaturated matrix and, hence $\frac{c_0}{c}$ is the supersaturation ration. As the degree of supersaturation increases, the chemical potential of the solute in the solution also increases, which in turn increases the thermodynamic potential for nucleation [9].

2.3.1.1 Homogeneous and Heterogeneous Nucleation

Nucleation causes a change in free energy (ΔG) of the system, which consists of three factors: the reduction of free energy from the formation of the new stable phase, the increase in free energy due to the formation of a new interface, and the increase in free energy from the deformation of the lattice. The change in free energy during nucleation is determined by the balance between the driving force for nucleation and the energy costs associated with creating a new phase, forming a new interface, and deforming the lattice. Therefore, this change is expressed:

$$\Delta G = V\Delta G_V + \gamma A + V\Delta G_\varepsilon \quad 2\text{-}2$$

Where V is the volume of the nuclei, γ is the interfacial energy and ΔG_ε is the strain energy. If we consider that the newly formed particles are spherical then the above expression transforms:

$$\Delta G(r) = \frac{4}{3}\pi r^3 \Delta G_V + 4\pi r^2 \gamma + \frac{4}{3}\pi r^3 \Delta G_\varepsilon \quad 2\text{-}3$$

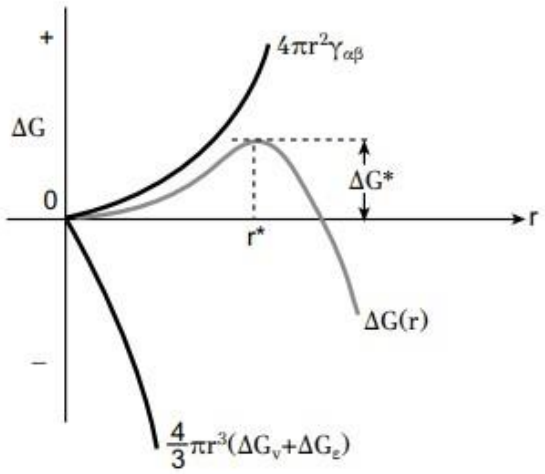

Figure 2-1: The change in free energy of the newly formed phase in relation to the particle radius during the process of nucleation.

In the above figure, r^* is the critical radius for nucleation. When particles increase in size up to the radius of r^*, they are referred to as embryos and they cannot grow any further. This leads to an increase in free energy. However, when the particles grow beyond r^*, they are known as nuclei and can continue to grow, lowering the free energy. Overcoming the activation energy barrier ΔG^* is required for nucleation, which is composed of interfacial and strain energies. For particles larger than r^*, the chemical driving force is dominant and contributes to the energy required for stable nuclei formation. r^* can be extracted from setting the derivative of ΔG equal to zero. Therefore:

$$r^* = -\frac{2\gamma}{(\Delta G_V + \Delta G_\varepsilon)} \quad 2\text{-}4$$

And

$$\Delta G^* = \frac{16\pi\gamma^3}{3(\Delta G_V + \Delta G_\varepsilon)^2} \quad 2\text{-}5$$

Homogeneous nucleation is the formation of new phases within a uniform parent phase without the involvement of any structural imperfections. During this kind of nucleation, it has been observed that the activation energy barrier is too high. On the other hand, heterogeneous nucleation is the formation of new phases facilitated by the presence of foreign particles or surfaces, such as dislocations, vacancies and grain boundaries, acting as nucleation sites. A portion of the energy linked to these defects is utilized to lower the activation energy for nucleation. That way, in the majority of cases, heterogeneous nucleation is predominant. However, there have been a few examples of homogeneous nucleation of equilibrium phases. Some examples are the Cu-Co system and the precipitation of Ni_3Al in nickel-rich alloys [9,13].

Along the precipitation process of a material, interfacial and strain energy compete to contribute to the activation energy. At the onset of nucleation, when the particles are still small, they are in complete coherence with the matrix. Although this state incurs high coherency strain energy, it is preferred due to the much greater interfacial energy that an incoherent boundary would cause. Beyond a critical particle size, the value of interfacial energy exceeds that of semicoherent circumstances, causing the system to relinquish its total coherency. The relationship between the coherency and the critical radius of the precipitate will be explained below [9,13].

A system that has coherency with the matrix, its free energy derives from the sum up of interfacial and the coherency strain energy:

$$\Delta G_{coh} = \frac{4}{3}\pi r^3 4\mu\delta^2 + 4\pi r^2 \gamma_{coh} \quad \text{2-6}$$

A system that either has lost its coherency, fully or partially, its free energy is obtained as follows:

$$\Delta G_{sem} = 0 + 4\pi r^2(\gamma_{coh} + \gamma_{sem}) \quad \text{2-7}$$

Where γ_{coh} is the coherent interfacial energy, γ_{sem} is the semicoherent interfacial energy, $4\mu\delta^2$ is the strain energy per volume, μ is the shear modulus of the matrix and δ is the lattice misfit. The latter is the difference between the lattice parameters of the two phases. When δ is large, the strains are increased, and the system loses coherency. For a constant δ, the equation of ΔG_{coh} and ΔG_{sem} gives the critical radius, r_c :

$$r_c = \frac{3\gamma_{sem}}{4\mu\delta^2}$$

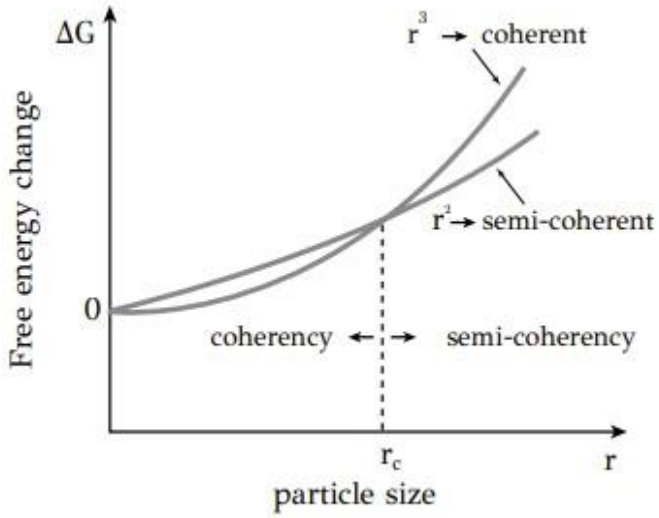

Figure 2-2: The correlation between the change in free energy and the size of particles, considering both coherent and semicoherent particles [9].

As it can be observed in the above figure, until the critical value of r_c the system prefers the coherent status because it lowers its free energy. For values greater than r_c, semicoherent interfaces are preferred. This procedure, referred to as coherency loss, begins during the nucleation regime and persists throughout the growth of the precipitates [9,13].

Despite that, dislocation loops have been observed to complicate coherency loss. This phenomenon can be fulfilled by different means. One of them is when the force endured by spherical precipitates surpasses the theoretical strength of the matrix (given that $\varepsilon_{crit} = 0.05$). Furthermore, it's possible that a dislocation loop crosses the precipitate's boundary, as indicated in Figure 2-3(a). No matter the size of the particle, this process will still go into effect. In contrast, another mechanism can come into play, in spherical precipitates, which involves dislocations being drawn to the particle's edge, forcing them to wrap around it. This process, shown in Figure 2-3(b), requires particle size to be bigger than r_c and it may be helped by mechanical forces during the aging process, but it doesn't take place in materials that have been annealed. Regarding plate-shaped precipitates, the reduction of coherency happens with dissimilar methods. The magnitude of the strain placed on the edges of the precipitate can surpass the matrix's theoretical strength, leading to the generation of dislocations. A major characteristic of this process is the ability to repeat itself multiple times as the plate is extended, which is shown in Figure 2-3(c). A process by which vacancies gather at coherent interfaces and create a prismatic dislocation loop that surpasses the precipitate can be seen in Figure 2-3(d).

During ageing, it was shown that the system preferred to precipitate, originally, incoherent or semicoherent phases that were previously called intermediate phases. That happened because the system wanted to reduce its free energy by losing coherency with the matrix.

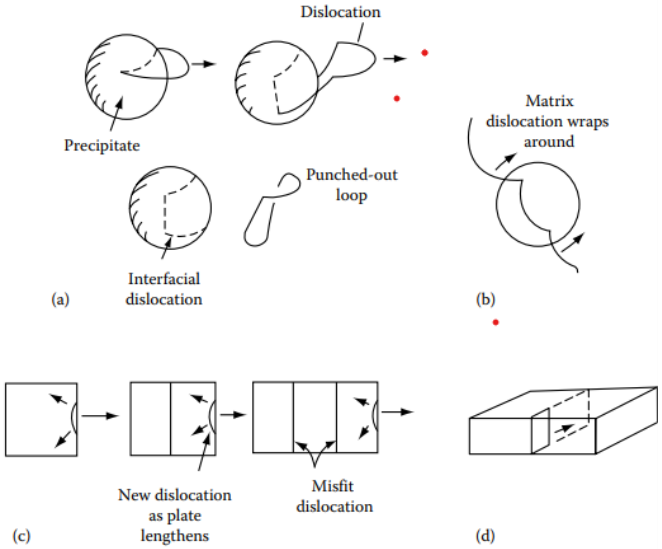

Figure 2-3. Coherency loss mechanisms. (a) Dislocation punching from interface. (b) Capture of matrix dislocation. (c) Nucleation at edge of plate repeated as plate lengthens. (d) Loop expansion by vacancy condensation in the precipitate [13].

Homogeneous nucleation could take place in every atom that exists on the matrix. On the other hand, heterogeneous nucleation sites involve structural defects. These include dislocations, grain

boundaries, vacancies, stacking faults and free surfaces. In most cases, nucleation happens heterogeneously as mentioned above. When a nucleus is created on these sites, free energy related to the defects is released and, therefore, reduces the activation energy.

$$\Delta G_{het} = V\Delta G_V + \gamma A + V\Delta G_\varepsilon + \Delta G_d \qquad 2\text{-}8$$

Where ΔG_d is the free energy of the defect and $\Delta G_d < 0$

The system prefers sites that have the potential to reduce the activation energy more than others. But it is not always the case as other parameters influence the sites that nucleation occurs. Such parameters are the precipitation driving force and the concentrations of these sites. Below, a table is presented of the different defects with their potential to reduce activation energy, from high to low.

Table 2-1: The arrangement of nucleation sites in descending order based on the decreasing activation energy for nucleation, from highest to lowest [13].

Nucleation sites
1) free surfaces
2) grain and interphase boundaries
3) stacking faults
4) dislocations
5) vacancies
6) homogeneous sites

Based on the table, nucleation is preferred on free surfaces and grain or interphase boundaries. However, in the case of a very high precipitation force, the homogeneous sites that are in the bottom of the above table, hence they have the lowest potential to reduce the activation energy barrier, are preferred because they have higher nucleation rates. If the driving force was low, the prevailing nucleation sites would indeed be the grain boundaries.

2.3.2 Vacancies and PFZs

Ageing temperature in aluminium alloys, as it has been already shown, is significantly lower than that of the solution treatment temperature. When the material is solution-treated the number of vacancies increase exponentially because of the temperature [13]. During the quenching, the system is not able to reduce its vacancy concentration to that of the equilibrium values. Therefore, there is an excess concentration of vacancies in the supersaturated solid solution. When the procedure of aging has begun, some vacancies will anneal out and some others will form VRCs, or vacancy rich clusters, by clustering with solute atoms [9,14].

Excess vacancies also, contribute to the increase of nucleation and growth of the precipitates by facilitating the diffusion of solute atoms to the matrix, thus raising the diffusional rates. This is how GP zones are formed in the Al-Cu alloys at low temperature in natural aging conditions. Furthermore, as mentioned earlier, high concentrations of clusters that surpass the equilibrium values enable them to be used as heterogeneous nucleation sites along the precipitation sequence.

Moreover, vacancies seem to have a significant involvement in the creation of PFZs or precipitate free zones. This defect forms during precipitation strengthening. It has been observed that after ageing, there are zones near the grain boundaries that have no precipitates. One possible explanation is the precipitation that is taking place on the grain boundaries. Grain boundaries are sites that favor heterogeneous nucleation and subsequent growth after quenching. Solute atoms are exhausted from the matrix phase and the aftermath is a PFZ [13,15]. Another theory is that grain boundaries operate as sinks and this time instead of solute being exhausted from the matrix, vacancies are being depleted. Along with the fact that vacancies act as nucleation sites, precipitation does not advance in these zones resulting in PFZs whilst the solute concentration is no different from the one inside the grain [9,13,15].

There are several measures that can be applied to eliminate or to limit the development of PFZs. One possible measure is to achieve a high driving force for precipitation and a low aging temperature. Due to supersaturation, homogeneous nucleation is feasible and is preferred by the system to vacancies. Another proposal is to cool the material as fast as possible. This way vacancies will not be consumed as if they would at slower quenching rates. A direct consequence of this is thinner PFZs.

2.3.3 Growth

This procedure follows nucleation. The growth is controlled by the phase diagram in the way that is concluded when the newly formed precipitate achieves the equilibrium concentration. The precipitate phase grows when its boundaries are moving inside the matrix and contains the movement of atoms from the matrix phase to the precipitate.

Growth can be broken down into two categories, depending on the interface between the precipitate and the matrix phase: glissile and non glissile. The difference between them is how the interface moves. In glissile interfaces, the movement is controlled by dislocation slide and no diffusion is needed. This category is met in martensitic transformations [9]. The second category is governed by diffusion and is the one that will be analyzed further for the purposes of this thesis.

Growth can be differentiated depending on the concentration of the precipitated phase and could be either under interfacial control, diffusional control, or both. When under interfacial control growth, the concentration is the same between the new phase and the matrix. In this case the diffusion rates are high, and it comes up to how fast the atoms traverse the interface. In diffusional-controlled growth, the reverse happens.

Figure portrays the precipitation growth sequence of an alloy. In Figure 2-4(a) the alloy is quenched from T_1 to temperature T_0. At first, the alloy is in phase α which is a homogeneous solid solution. After the quench in T_0, phase α is supersaturated and has a driving force for precipitation of phase β. The next diagram depicts the free energy of the two phases. There is a chemical driving force for precipitation of phase β equal to the line segment of TL. In Figure 2-4(c) the concentration profile of B element along the growth process is presented. The concentration of the precipitated phase is constant with the value c_β. In the interface, this value drops instantaneously, in c_i. Here it is important to note that the precipitate grows by diffusing B atoms from the supersaturated matrix to the newly formed phase β. For the phase α, at the interface, the concentration is c_i which is different from the value that the thermodynamic equilibrium imposes. If that was the case, growth would be under diffusional control. On the other hand, if the concentration was equal to the supersaturated concentration, c_0, that would manifest interface-controlled growth. In this case, c_i is between these two values and both mechanisms take place at the same time [9,13].

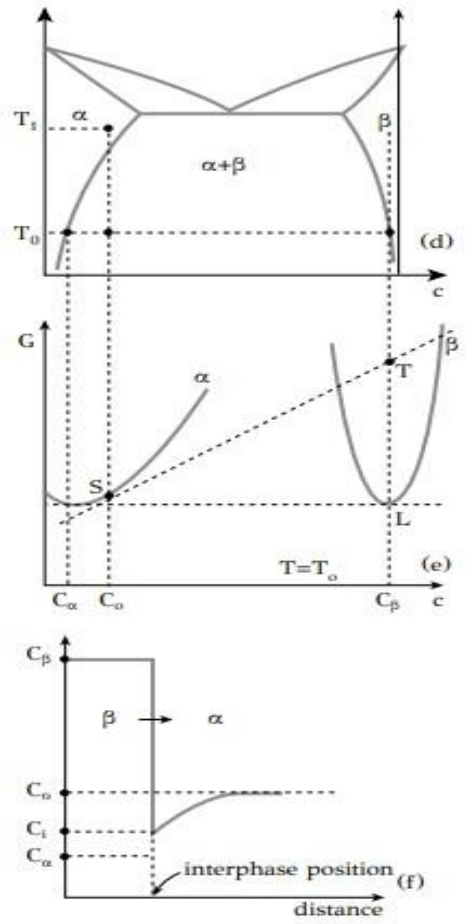

Figure 2-4: (a) Phase Diagram, (b) free energy at T_0, (c) concentration profile [13].

2.3.4 Precipitation Kinetics

As previously indicated, the development of a new phase constitutes of two processes: nucleation and growth. Most of the times, these two mechanisms take place simultaneously, i.e., in the time that new particles nucleate others are growing. Therefore, this interplay impacts the overall conversion rate.[9,13]

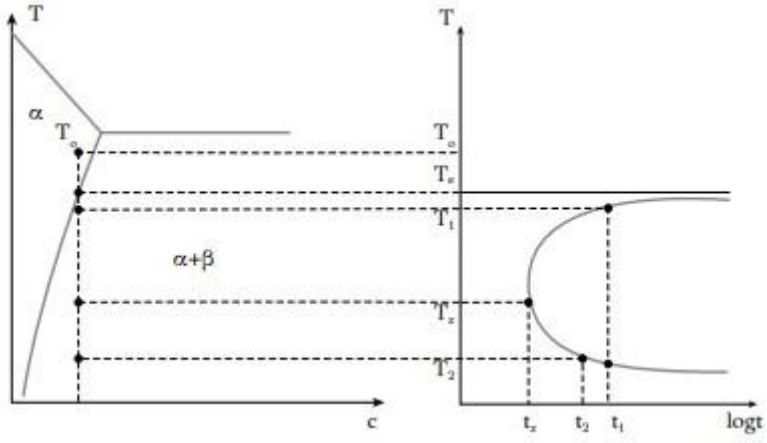

Figure 2-5: The rate of diffusional transformation as a function of temperature [9].

These transformations that take place can be embodied in a C-type curve. Figure 2-5 presents an example of various transformation rates. The first thing that is noticeable is that the overall kinetics are temperature dependent. When precipitating at relatively high temperatures, such as T_1, diffusion rates are high, but the driving force is low because supersaturation has not been achieved. This leads to slow transformation rates. Identically, when supersaturation is achieved in low temperature T_2, diffusion is slow, and the transformation rate is identical to temperature T_1. Consequentially, it obvious that the maximum transformation rate is accomplished at temperatures between T_1 and T_2, where both driving force and diffusivity are combined optimally [9,13].

Using the C-type curves, we can go a step further by defining the transformation fraction f which is a function of time and temperature:

$$f = \frac{f_\beta}{f_\beta^{eq}} \qquad 2\text{-}9$$

Where f_β is the volume fraction of the precipitated phase and f_β^{eq} is the equilibrium volume fraction of the precipitated phase. f takes values from 0 to 1 when the transformation begins and when it ends, respectively.

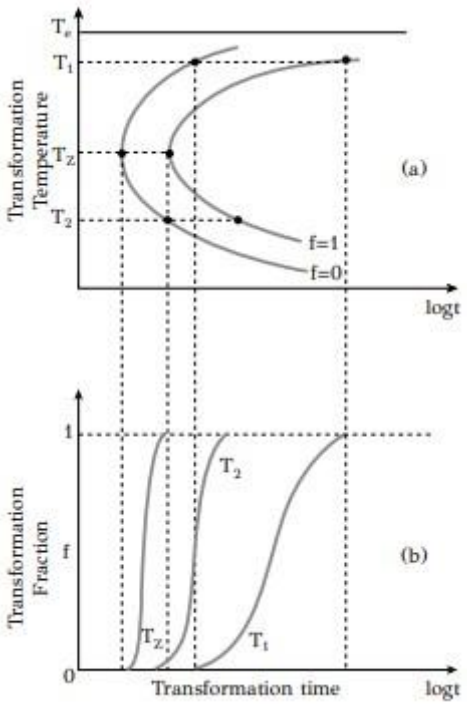

Figure 2-6: (a) IT (isothermal transformation) diagram, (b) Fraction function for three different temperatures

In Figure 2-6 (a) a TTT (Transformation Temperature Time) diagram is presented in comparison with f function which is depicted in Figure 2-6(b). The TTT diagram, which is based on the C-curve diagram and the f function, is comprised of two C-curves. The left one depicts the start of the transformation while the right one shows the end. The evolution of the precipitated phase transformation is shown for the same temperatures as Figure 2-5. As can be noticed, the fraction function has a characteristic S shape and can in fact split into three time intervals, as shown in Figure 2-7 [9,13].

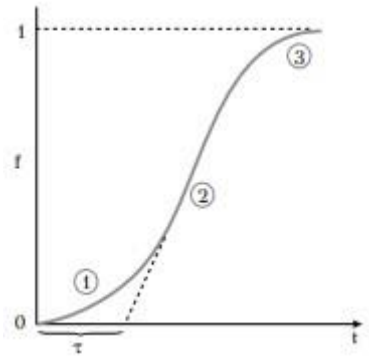

Figure 2-7: An S-curve consisting of 1: induction period, 2: growth period and 3: impingement period [9].

Induction is the first period, during which nucleation occurs and ends after τ time. The next process that takes place is precipitate growth and concludes slightly prior to the completion of the transformation. Finally, the third and final stage is the one of the impingement. During this procedure, growth rates decrease, because the precipitates have reached a size that is possible for them to meet, and eventually nullify.

To conduct a mathematical evaluation of the transformation kinetics, some assumptions have to be made. Firstly, it is presumed that the precipitates have a spherical shape. Also, the volume that is taken by phase α is, finally, occupied by the precipitated phase. If steady nucleation rate is assumed, the transformation fraction can be explained by the following formula:

$$f = \frac{\pi}{3} N v^3 t^4 \qquad 2\text{-}10$$

where N is the nucleation rate, t is the time and v is the growth rate. This formula describes well the volume development of the precipitates but does not consider impingement [9,13]. An equation that includes the decrease in growth rates by the phenomenon of impingement was developed by Johnson-Mehl [16]. This model is based on the hypothesis that a precipitate can grow into an already formed one- and this-way impingement can not take place. The new theoretical volume is different from the actual volume. This way, the relation of these two volumes is given by Johnson-Mehl equation:

$$-\ln(1-f) = \frac{4}{3}\pi v^3 \int_0^t N(t-\tau)^3 \, d\tau \qquad 2\text{-}11$$

Certain speculations have to be made concerning the nucleation rates in order for this equation to be solved. If we assume steady rate for nucleation, then this relation turns into:

$$f = 1 - \exp\left(-\frac{\pi}{3} N v^3 t^4\right) \qquad 2\text{-}12$$

Generally, nucleation rates are not steady. A more general equation that can be applied in a wide range of scenarios including not constant nucleation rates is the JMAK [17] :

$$\mathrm{f} = 1 - \exp\left(-\mathrm{kt}^{\mathrm{n}}\right) \qquad 2\text{-}13$$

where k is dependent on growth and nucleation rates. n values are given by the following table [13]:

Table 2-2: Different values of n-exponent in the JMAK equation [9,18].

	Interface-Controlled	Diffusion-Controlled
Constant nucleation rate	4	2.5
Nucleation rate increasing	>4	>2.5
Nucleation rate decreasing	3-4	1.5-2.5
Saturation of nucleation sites	3	1.5
Grain edges nucleation	2	1
Grain surfaces nucleation	1	0.75

2.3.5 Coarsening

After the precipitating phase has formed by nucleation and growth, the system is assumed to have reached an equilibrium. The fractions of the matrix and the precipitated phase are given by the phase diagram, by applying the lever rule. Nonetheless, equilibrium has not been achieved yet and the system is still in an intermediate situation. This happens because the interfacial energy between the two phases has not been minimized. In order for this to happen, the system does two things. It reduces the number of available precipitates and increases their size. This procedure is called coarsening and generates some unwanted effects such as the reduction of strength. Coarsening is also tightly controlled by temperature. As temperatures increase so does the coarsening speed [9,13].

A way to comprehend and govern this phenomenon is to examine its kinetics and thermodynamics. As mentioned earlier, the driving force for coarsening is the reduction of the interfacial energy [9]. The Gibbs-Thomson effect [19] relates free energy with the radius of a particle. The formulation of this effect is given below. As the radius increases, the free energy decreases. When growth is concluded, the microstructure of the material consists of a broad range of precipitates with different sizes due to the distinct growth rates. The material, in order to reduce the free energy, shrinks smaller precipitates by diffusing solute atoms to the larger ones which grow in size [9].

$$\Delta G = \frac{2\gamma V_m}{r} \qquad 2\text{-}14$$

Where γ is the interfacial energy, V_m is the molar volume of the precipitated phase and r is the radius.

In Figure 2-8(a), the free energy curves in relation to the concentration of the matrix and the precipitate phase, for various radiuses, are presented. Firstly, the curve with r_∞ is when the system has reached equilibrium, as portrayed in the phase diagram. The other two curves depict two possible metastable statuses with different curvatures, where r_2 is smaller than r_1. As noted previously, the precipitate with r_2 radius has a higher free energy than the one with $r_1$radius. This free energy

difference, between the metastable precipitates and the equilibrium one, is the driving force for B atoms diffusion from the smaller to the larger particles [9,13].

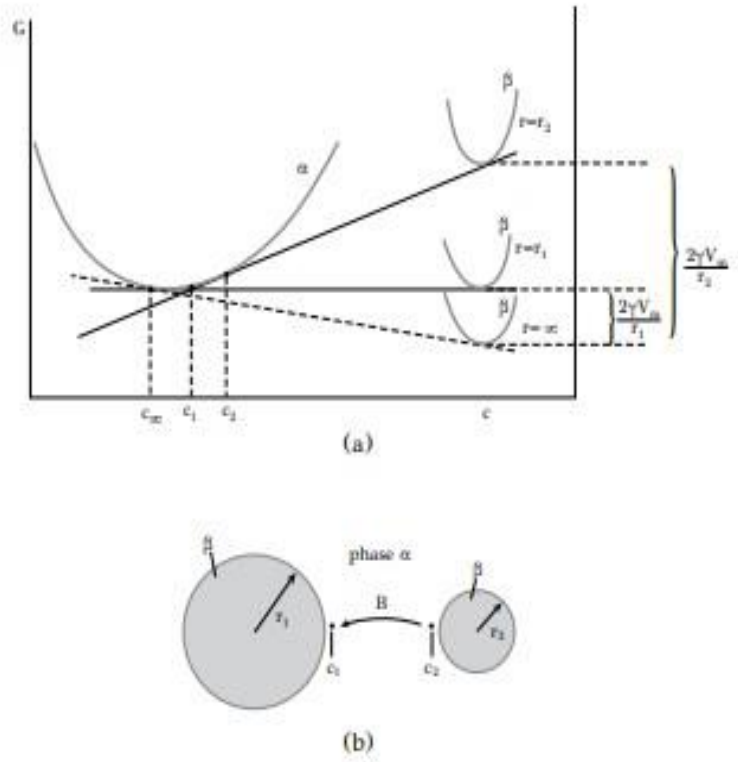

Figure 2-8: (a) Free energy and the concentration of the α and β phases, considering different values of the curvature radius of the β phase particles, (b) B atoms diffuse from smaller to bigger particles [9].

Greenwood [20] was able to quantify the pace at which the radius of precipitates increased while researching the kinetics of coarsening. The coarsening rate, based on his work, is given by the following equation:

$$\frac{dr}{dt} = Dc_{\infty}\frac{2\gamma V_m}{kT}\frac{1}{r}\left(\frac{1}{\bar{r}} - \frac{1}{r}\right) \qquad 2\text{-}15$$

Where D is the diffusional coefficient, c_{∞} is the concentration of the matrix phase as depicted in the phase diagram and $\bar{r}$ is the mean radius of the dispersion. In the following figure (Figure 2-9), two coarsening rates with different mean radiuses are compared.

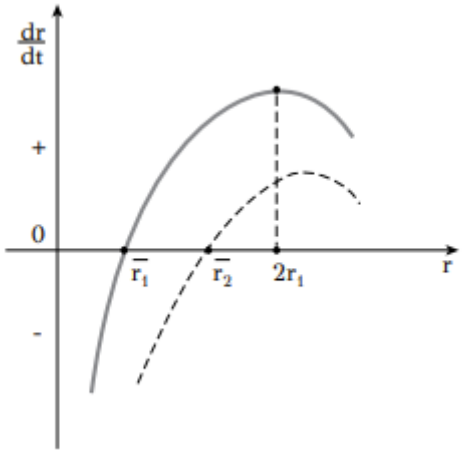

Figure 2-9: The relationship between coarsening rates and radius for two distinct mean radius values, as described by the Greenwood [9].

It is noticed that the coarsening rates assume negative values for radiuses less than the mean radius value. This indicates that the precipitates, in this instance, lose solute atoms thus they decrease in size. In contrast, the coarsening rates are positive for precipitates with a radius greater than the mean, and as a result, the precipitates coarsen by taking in the solute atoms from the particles that shrink. Another observation is that the dispersion with $\bar{r}_1$ radius have higher coarsening rates than the one with $\bar{r}_2$. Finally, the fastest rate of coarsening occurs when the radius takes values approximately 2 times the mean value [9,13].

Lifshitz and Slyozov [21] along with Wagner [22] developed the LSW theory. This theory explains how the mean radius of a dispersion is changing with time by applying coarsening kinetics. The formula of this theory is given by the following equation:

$$\bar{r}^3 - \bar{r_0}^3 = \frac{8D\gamma V_m c_\infty}{9kT} t \qquad 2\text{-}16$$

Where $\bar{r_0}$ is the distribution of the mean radius prior to coarsening. It is evident that the coarsening speed is affected by the strong dependence of temperature, as both the diffusion coefficient and the c_∞ increase at exponential rates with T [9].

2.4 Precipitation Strengthening Mechanisms

Precipitation hardening is a process utilized by different alloy systems i.e., steels, titanium, and aluminum to enhance their strength. This happens by impeding the movement of the dislocations through the introduction of finely dispersed precipitates which form accordingly to the phase diagram. In some cases, this mechanism leads to considerable hardening that overshadows other strengthening mechanisms present in the alloy [9]. The aluminium alloy 2024 studied in this thesis obtains its strength through the precipitation of the intermetallic S-phase [5–7,23–26]

On that note, there is a relation between the dislocations and the coherency of the transient phases during the precipitation process. As mentioned earlier, when aging starts, the particles formed are coherent to the matrix phase. These are prone to be penetrated by dislocations. The stress fields created by the dislocations interact with the coherency strain fields and the result is the obstruction of the dislocations' movement. This in turn results in hardness increase which is depicted in the following equation:

$$\Delta\tau = k_1 f^{\frac{1}{2}} r^{\frac{1}{2}} \quad \text{2-17}$$

Under certain circumstances, coherent particles can display a structured arrangement. In such instances, there is a localized interaction between the precipitate and a dislocation. When the dislocation enters the ordered particle, it generates an anti-phase boundary (APB) on the plane where slide occurs. This interaction is expressed as follows:

$$\Delta\tau = k_2 \gamma_{APB}^{\frac{3}{2}} f^{\frac{1}{3}} r^{\frac{1}{2}} \quad \text{2-18}$$

Where k_1 , k_2 are constants, f is the volume fraction of the particles and r is the mean radius. γ_{APB} is the interfacial energy of the boundary. APBs have significantly increased interfacial energy and this emerges as strength increase [9].

When it comes to semicoherent or incoherent particles, they cannot be penetrated by dislocations. The Orowan mechanism allows dislocations to overcome these particles. A pair of neighboring precipitates can be seen as a Frank-Reed dislocation source where the gliding dislocation curves amidst an array of precipitates. In Figure 2-10, there is a visual representation of this mechanism. As the dislocation bends around the precipitates, its opposite points cancel each other, resulting in the formation of a dislocation loop. The stress required for a dislocation to exceed these particles, is:

$$\tau_{max} = \frac{\mu b}{L} \quad \text{2-19}$$

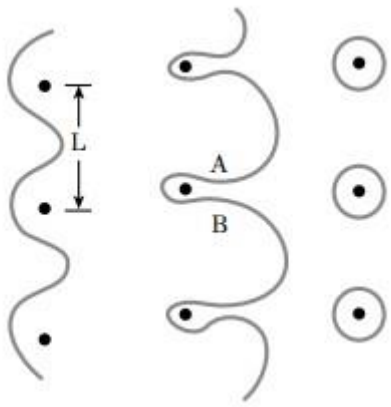

Figure 2-10: Orowan mechanism

Where L is the distance between them. As loops are formed, the distance between dislocations decreases which in turn results in higher stress levels for them to surpass the precipitates. This increase in the stress required leads to a phenomenon known as strain hardening. This procedure has been named Orowan by-passing and the hardening that takes place is called Orowan hardening. The relation of this mechanism with the fraction, f, and the size of the particles, r, is the following:

$$\Delta\tau = k_3 f^{\frac{1}{2}} r^{-1} \quad 2\text{-}20$$

As it has been depicted in the previous equations, the strengthening factor depends heavily on the size of the particles. At the beginning of precipitation hardening, when particles are coherent, the strength increases accordingly to $r^{\frac{1}{2}}$, while at later stages, it is proportional to r^{-1}. In Figure 2-11, the two different mechanisms are pictured as a function of hardness and particle size. Note that, the highest gain of hardness is achieved when the coherency strengthening mechanism transitions to Orowan's.

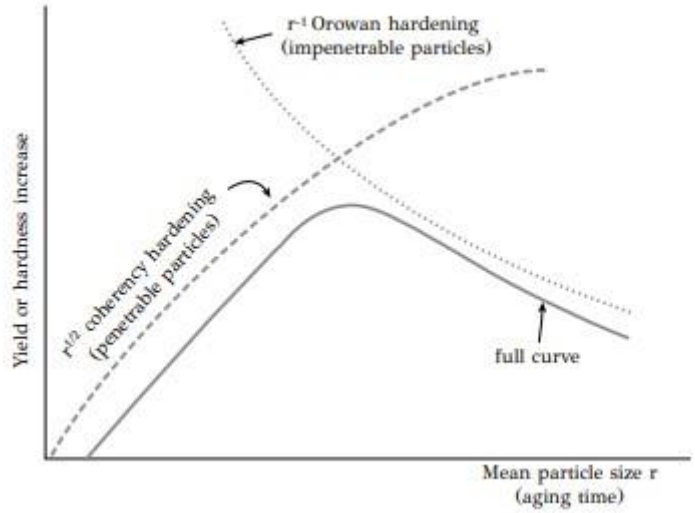

Figure 2-11: The enhancement of strength due to the presence of penetrable and impenetrable particles, considering the size of the particles or the aging time.

2.5 Other Strengthening Mechanisms

2.5.1 Cluster Hardening

One of the main hardening mechanisms in AA2024, apart from precipitation hardening of the S phase, is hardening due to Cu-Mg clusters. These clusters are coherent with the matrix phase and thus the Orowan mechanism explained earlier is not applicable. Instead, various strengthening mechanisms associated with obstacle shearing must be considered. These mechanisms include order, modulus and chemical hardening [8,27–30]. However, as these clusters uphold the matrix structure and no internal ordering is present, order strengthening is very restricted [8]. Thus, these alloys appear to be hardened, mainly, by the mechanism of modulus strengthening which has been found challenging to handle theoretically. This is mainly due to the fact that there are not any systems that, primarily, obtain their strength by this mechanism and the different theories that have been proposed cannot be tested experimentally [8,31,32].

In many works [8,25,27–29,33], the equation from Cartaud et al. has been used. The modulus strengthening is given by the following relation:

$$\Delta\tau = \frac{\Delta\mu}{4\pi\sqrt{2}} f_{cl}^{1/2} \quad \text{2-21}$$

Where $\Delta\mu$ is the difference between the shear modulus between the aluminum rich matrix and the clusters, μ_{cl} and f_{cl} is the volume fraction of the clusters.

For the calculation of $\Delta\mu$, μ_{cl} has to be determined. The most accurate way is by calculating the weighted average of moduli of the distinct elements [8,28,33] and is given by the following expression:

$$\mu_{cl} = x_{Cu}\mu_{Cu} + x_{Mg}\mu_{Mg} + x_{Al}\mu_{Al} \quad \text{2-22}$$

Where x is the fraction and μ is the shear moduli of the distinct elements.

2.5.2 Chemical Hardening

As far as chemical hardening is concerned, its contribution is, also, very limited. Brown and Ham [8,32] have estimated this contribution and is as follows:

$$\Delta\tau_{ch} = \left(\frac{6bf}{\pi\Gamma}\right)^{1/2} \frac{\gamma^{3/2}}{r} \quad \text{2-23}$$

And

$$\Gamma = \beta_{LT}\mu_{Al}b^2 \quad \text{2-24}$$

Where Γ is the dislocation line tension. β_{LT} is a constant. The rest of the values are known and have been discussed before. If a radius in the range of 0.5-0.7nm, an interfacial energy of 0.07 J/m^2 and a fraction of 0.05 is assumed, then the contribution of the chemical hardening is in the range of 3-5 MPa. This value is small; 3-5% of the contribution the modulus hardening mechanism [8,28,33].

2.6 Precipitation in 2xxx series of Aluminum Alloys

The precipitation of 7xxx aluminum alloys has been the subject of extensive investigations for many years, owing to the high strengthening potential they exhibit and the complex mechanisms that govern this transformation. However, the morphologies of the precipitate phases and their transitional relationships remain controversial subjects for the scientific community. In the following paragraphs, a review of the precipitation phases and their transformations in Al-Zn-Mg-Cu alloys will be presented.

2.6.1 Precipitation Sequence in 2xxx series of Aluminum Alloys

The aluminum alloys belonging to the 2xxx series obtain their properties by the procedure of heat treatment. These properties are the end result of the different precipitation sequences that might

occur. In particular, two precipitation sequences have been identified depending on the composition of the alloys and the ratio of the main alloying elements (Cu/Mg ratio)[3,6,8,34,35].

For alloys with a high Cu/Mg ratio with values between 4 and 8, the precipitation sequence is the following [8] :

$$\text{SSSS} \rightarrow \text{GPI zones} \rightarrow \text{GPII/ } \theta'' \rightarrow \theta' \rightarrow \theta \ (Al_2Cu)$$

This is the same with Al-Cu alloys and will not be investigated further as part of this thesis. For aluminum alloys that have low to medium Cu/Mg ratio, such as 1.5 to 4, this sequence has been expressed as:

$$\text{SSSS} \rightarrow \text{GPB zones/Cu-Mg clusters} \rightarrow S'' \rightarrow S' \rightarrow S \ (Al_2CuMg)$$

Where SSSS is the super saturated solid solution, GPB are the Guinier Preston Bagaryatsky [36] zones and S''/S' are the metastable phases that lead to equilibrium one. This is the sequence that will be analyzed in detail as in this thesis the aluminum alloy 2024 is studied. Finally, for alloys with a Cu/Mg ratio higher than 8, T-phase (Al_6CuMg_4) and β-phase ($Al_{12}Mg_4$) appear with a rapid decrease in mechanical properties [6].

The majority of the studies in AA2024 series have observed that strengthening occurs in two stages. The initial hardening is credited to GPB zones/Cu-Mg clusters while the peak strength is achieved at a later stage during the precipitation of S-phase[1,3–9,13,23–26,28,29,34,35,37,38].

2.6.1.1 GPB Zones and Cu-Mg Clusters

Bagaryatsky [36] and Silcock [39] were the first to observe the GPB zones during precipitation on similar composition alloys. Silcock, also, suggested that they had a cylinder morphology with a diameter of 1-2mm and a length of 4-8mm [3,8]. The early hardness increase in 2024 alloy is attributed to these zones, which are coherent with the matrix as they are the first metastable phase.

Later works tried to find evidence of the existence of these zones, with the use of technology that was not available earlier such as TEM, HREM and SAD [8,40–44]. These failed to find any characteristics that GPB zones are known for or criticized earlier publications that had found evidence of their existence [26]. The microstructure of the alloy Al-0.9Cu-1.4Mg, aged for 4 hours at 200°C, was studied by Charai et al. [45]. This study found that Mg clusters and Cu platelets coexisted. The latter were recognized as GPB zones. However, for the same composition and methodology as Charai et al., Zahra et al. [40] could not distinguish the GPB zones. It is worth mentioning that the same researchers that identified the Mg clusters in [45], in earlier works [40] the same clusters were recognized as GPB zones. It is obvious that there is a dilemma between the existence of GPB zones and clusters. Another group of researchers, Radmilovic et al. [46], observed the existence of Cu-Mg clusters during the aging of the aluminum alloy Al-2.0Cu-1.1Mg for 72 hours at 190°C. These were found to be similar to the Mg clusters found by Charai et al. The above clusters compared with the GPB zones found by Ringer et al.[47] were, actually, found to be identical with respect to shape, size composition, degree of order and orientation [8].

Even more studies using more advanced techniques, such as 1DAP, 3DAP and atom probe field ion microscopy (APFIM) identified the clustering of atoms right after the quenching process and before the forming of other metastable or stable phases [43,47–50]. More specifically, in the Al-1.1Cu-1.7Mg alloy Cu clusters and Mg clusters were found immediately after the quench while Cu-Mg clusters were identified after 5 minutes of aging at 150°C [8,28,47]. Some other researchers observed the formation of small Cu-Mg clusters by 3DAP in two alloys that were stretched and aged for 12h at 150°C. Their size

was in the range of 0.7nm to 0.8nm while the concentration of the solute atoms were 30% for both the Cu and Mg with the rest 40% occupied by aluminum [43,44]. Moreover, findings from multiple studies utilizing APFIM and 3DAP indicate the presence of Cu-Mg clusters with a diameter close to 1nm [28,33,47,51].

Cu-Mg clusters and GPB zones, as mentioned earlier, exhibit complete coherence with the aluminum matrix and at the same time have identical compositions and shape, so the distinction between them presents a formidable challenge. This challenge is further compounded by employing various experimental techniques to characterize and identify them [8]. What is more, the term GPB zones was first used in the 1950s and has been utilized without substantial knowledge of its nature along with the development of newer techniques have led many investigators to not use this term. Instead, Cu-Mg clusters has been found to be more accurate[8,28].

2.6.1.2 S''-S'-S PHASE

There is controversy surrounding the presence and attributes of the S" phase. Bagaryatsky [36] was the first to identify this phase. He suggested an intermediate, coherent phase among GPB zones and S' phase. In many later works, the existence of this phase was confirmed with the use of TEM and HREM, but with distinct structure models [40–42,45,52]. Other researchers did not find any evidence of the existence of this metastable phase and suggested that the diffraction spots that were linked to S" phase were actually different variants of the stable S phase [51]. Silcock [39], in his findings, did not find any resemblance to the S" phase found by others and suggested that over 200°C, GPB2 zones were formed. Wang [53] and Starink [54] noted that all previous findings from the above researchers were the same structure named GPB2/S''[8].

When it comes to S' phase, there is no difference with the equilibrium S phase as noted by several researchers [3,8,23,25,34,35,38]. These two phases share the same chemical composition, formation enthalpy and crystal structure [8]. The only difference noted by all researchers is the lattice parameter. Therefore, there is no reason to distinguish S' phase from S phase.

The equilibrium S phase was suggested that it has an orthorhombic structure with space group *Cmcm* with lattice parameters a = 0.400 nm, b = 0.923 nm and c = 0.714 nm [3,8]. Also, two different types of S phase have been identified. These coexist and nucleate to one another. S-I phase has the orthorhombic structure mentioned while the S-II phase has a monoclinic structure [2,34]. Nucleation occurs heterogeneously on dislocation loops and helices while grain boundaries and solute clusters are, also, potential nucleation sites [8].

2.6.2 Alloying Elements

The presence of alloying elements contributes crucial properties that assist in the processing and strengthening of aluminum. Copper, magnesium, and zinc additions achieve enhanced strength by utilizing solid solution strengthening and precipitation hardening. Moreover, during heat treatment, these elements interact with the aluminum matrix to form intermetallic precipitates such as Al_2Cu and Al_2CuMg that enhance both strength and fatigue resistance [10]. In addition, other elements such as manganese and chromium, in small amounts, generate disperoids that impede grain growth leading to an increase of the yield strength. Small titanium amounts in the order of 0.1% help, also, with the reduction of the grain size.

Additionally, the inclusion of certain alloying elements such as cadmium and silicon significantly influence the age hardening of aluminum alloys. These play a crucial role in enhancing mechanical properties [8,55]. Many commercially available 2xxx aluminum alloys contain trace amounts of silicon

and iron. The presence of these elements leads to the formation of coarse intermetallic compounds, which negatively impact fracture toughness. However, minor additions of silicon less than 0.5% significantly enhance the response to age hardening at elevated temperatures [8,10,55]. Moreover, the addition of silicon serves to decrease the viscosity of molten aluminum, facilitating the casting process of intricate and bulky shapes without the formation of voids. On the other hand, Fe is employed to minimize hot cracking during casting [10].

Chapter 3 Methodology

3.1 Material Studied

In the preceding discussion, the research primarily concentrated on aluminum alloys from the 2xxx series, specifically alloy 2024 T3. The material was acquired in the form of plates, without undergoing anodization, and its sole surface protection was provided by a thin protective oxide layer formed when the material came into contact with the atmosphere. Multiple suppliers were sourced to obtain the material, with a thickness of 3.2mm.

The chemical composition of the alloy is depicted in Table 3.1.

Alloy	Al	Cu	Mg	Mn	Si	Fe	Cr	Zn	Ti	Other
2024	90,7-94,7%	4%-4.9%	1.2%-1.5%	0.6%	0,50%	0,5%	0,10%	0,25%	0,15%	0,15%

3.2 Heat Treatment and Microhardness Values

No experimental procedures took place for the purposes of this thesis. However, several experimental data as microhardness measurements were obtained from previous research of the Laboratory of Materials. Kefalas [56], Floratos [57] and Karantonidis [58] heat treated this alloy at the range of 490-495^{o}C for 30 minutes. Then, the specimens were aged artificially at 150^{o}C, 160^{o}C, 170^{o}C and 210^{o}C in an electric oven with ±5^{o}C temperature control and for different times. For every different heat treatment, multiple measurements were conducted at different aging times to determine the maximum hardness level. For the temperature of 150^{o}C, the aging times were 8 h, 12 h, 24 h, 48 h, 72 h, 96h, 120h and 384h. For the temperature of 160^{o}C, the aging times were 8 h, 12 h, 24 h, 48 h, 72 h, 96h, 120h. In addition, for the 170^{o}C, the corresponding times were 1h, 4h, 6h, 9h, 12h, 15h, 24h, 48h, 63h and 98h. Finally, for the 210^{o}C, the times are 1h, 4h, 6h, 12h, 15h, 24h, 48h and 63h.

3.3 Modeling Precipitation with KW numerical method

For the investigation of the precipitation-induced microstructural phenomena and strengthening evolution of the 2024 aluminum alloy, the TC-PRISMA module was used to simulate the heat treatment process of one-step aging. This module is built-in the computational software of Thermo-Calc and employs the Kamppman-Wagner numerical analysis along with the Langer-Schwartz theory to simulate precipitation in complex alloy systems, predicting particle size and volume fraction evolution. Through integration with the DICTRA module, all the necessary KWN model parameters are calculated accurately. To obtain the necessary thermodynamic and mobility parameters, TCAL7 and MOBAL5 databases were used, respectively.

3.3.1 KW Methodology

The KW model explains the precipitation kinetics by utilizing the nucleation and growth mechanisms to reduce the Gibbs energy of the system towards a state of mass equilibrium. In this model, the evolution of the PSD over time is directly solved by discretizing it into size classes. The process involves two steps per simulation cycle: firstly, the classical nucleation theory is used to determine the quantity

of new particles generated, and secondly, these particles are assigned to the relevant size group. The nucleation rate for multicomponent alloy systems is:

$$J(t) = J_S \exp\left(-\frac{\tau}{t}\right) \quad 3\text{-}1$$

Where J_S is the steady state nucleation rate, τ is the incubation time for establishing steady state conditions and t is the time.

$$J_s = NZ\beta^* \exp\left(-\frac{\Delta G^*}{kT}\right) \quad 3\text{-}2$$

Where N is the number of the available nucleation sites per unit volume, Z is the Zeldovich factor, β^* is the atomic attach rate, ΔG^* is the Gibbs energy of formation, k is the Boltzmann's constant and T is the absolute temperature. ΔG^* can also be referred as the nucleation barrier and can be written as:

$$\Delta G^* = \frac{16\pi}{3} \frac{\gamma^3 V_m^2}{\left[\Delta G_m^{\alpha\to\beta}\right]^2} \quad 3\text{-}3$$

Where γ is the interfacial energy, V_m is the molar volume of the S phase and $\Delta G_m^{\alpha\to\beta}$ is the maximum driving force for the α → β transformation. The Zeldovich factor can be extracted from the following equations:

$$\mathrm{Z} = \frac{\mathrm{V_m}}{2\pi \mathrm{N_A} \mathrm{r^{*2}}} \sqrt{\frac{\gamma}{\mathrm{k_\beta t}}} \quad 3\text{-}4$$

Where r^* is the radius of the critical nucleus and $\mathrm{N_A}$ is the Avogadro number. The critical radius for nucleation derives from the following equation:

$$\mathrm{r^*} = -\frac{2\gamma \mathrm{V_m}}{\Delta \mathrm{G_m^{\alpha\to\beta}}} \quad 3\text{-}5$$

For the calculation of the growth rate, the Simplified Growth Model [59] by Morral and Purdy was used in TC-PRISMA Precipitation module. Using this model, which makes the assumption that conditions are in a state of pseudo-steadiness, the growth rate can be determined through the following set of equations:

$$v(r) = \frac{K}{r}\left[\Delta G_m - \frac{2\gamma V_m}{r}\right] \quad 3\text{-}6$$

and

$$K = \left[RT\sum_i \frac{X_i^{\beta}(r) - X_i^{a}(r)}{X_i^{a}(r) M_i}\right]^{-1} \quad 3\text{-}7$$

Where ΔG_m is the nucleation driving force, K is a kinetic parameter, $X_i^{\beta}(r)$ is the mole fraction of the precipitate's phase, $X_i^{a}(r)$ is the mole fraction of the matrix phase and M_i is the atomic mobility. To complete the methodology, the continuity equation of the PSD [60] has to be solved. It can be expressed as:

$$\frac{\partial f}{\partial t} + \frac{\partial}{\partial r}[v(r) f(r)] = g(r) \quad 3\text{-}8$$

Where f is the PSD function and $g(r)$ is the distributed nucleation rate, which is defined by the subsequent equation:

$$J(t) = \int_{r^*}^{\infty} g(r) dr \quad 3\text{-}9$$

Due to its complexity, the continuity equation of the PSD has to be solved numerically. TC-PRISMA applies the numerical method of characteristics, where the number of particles in the same size class changes when same size particles are nucleated.

3.3.2 Utilizing TC-PRISMA module to simulate aging in the experiment

For precise precipitation modeling in the alloy, it is crucial to establish the right set of conditions. The matrix phase was FCC phase and S-phase, and S'-phase were assumed as the only hardening phase. The precipitation was modeled at the ageing temperatures of 150°C, 160°C, 170°C and 210°C, respectively. The S phase in the TCAL7 database is represented as S_PHASE, while the S' phase as S_PRIME. The precipitate of S phase was hypothesized to be sphere-shaped. Calculations were, also, carried out assuming needle-shaped morphology with an aspect ratio of 10 [8,25]. The average grain size of the FCC phase and the average grain aspect ratio was assumed 100μm and 1 [1], correspondingly. Nucleation was assumed to be bulk-dominated with the number of nucleation sites set to default value.

As the simulation starts from the as-quenched state of the material, several prefactor values were used to approximate the necessary time for peak hardness. The prefactor is applied to the mobility data, scaling it by a specific amount to enhance the mobility calculation.

One of the most vital parameters in the model is the interfacial energy of the S phase precipitates. No available values were found in the literature. The development of this model was challenging in predicting the strength at varying ageing temperatures with constant interfacial energy. Using constant interfacial energy, strength values would increase notably with decreasing temperature due to an increase in the maximum number of precipitates which comes into contradiction with the experimental data showing minimal changes in peak strength at different aging temperatures [25]. In some recent works, temperature dependance of the interfacial energy has been discussed and, in this work, yielded accurate results. Khan et al. [25] has proposed the following formula for the interfacial energy during the nucleation regime:

$$\gamma_n = \gamma_{n,0} - aT^3 \qquad 3\text{-}10$$

Where γ_n is the interfacial energy (J/m^2), $\gamma_{n,0}$ and a are constant values with 0.1206 J/m^2 and 2.186 × 10^{-10} J/m^2 K^3 each. The simulation assumed an aging time of 1000 hrs. Then, the yield strength and microhardness values were obtained using the simplified yield strength model.

Chapter 4 Results

4.1 Microhardness Measurements

To enhance the clarity of the findings' portrayal, the measurements were graphed based on aging time, in hours, for each heat treatment, as explicitly mentioned earlier. In the following graphs, the measured hardness values for the 4 different aging temperatures of 150°C, 160°C, 170°C and 210°C are shown compared to the experimental procedures of Kefalas, Floratos and Karantonidis [56–58].

For the 150°C, as depicted in Figure 4-1, the findings are not in that good of accordance during the initial stages. Microhardness reaches the value of 154HV in 8 hours and remains nearly identical until the 96h mark. Kefalas in his thesis found out that the maximum hardness of 154.65 HV was reached in 120 hours, which did not change significantly compared to the value of the 48 hours mark. During the coarsening regime, the results become more accurate and, in some cases, almost identical.

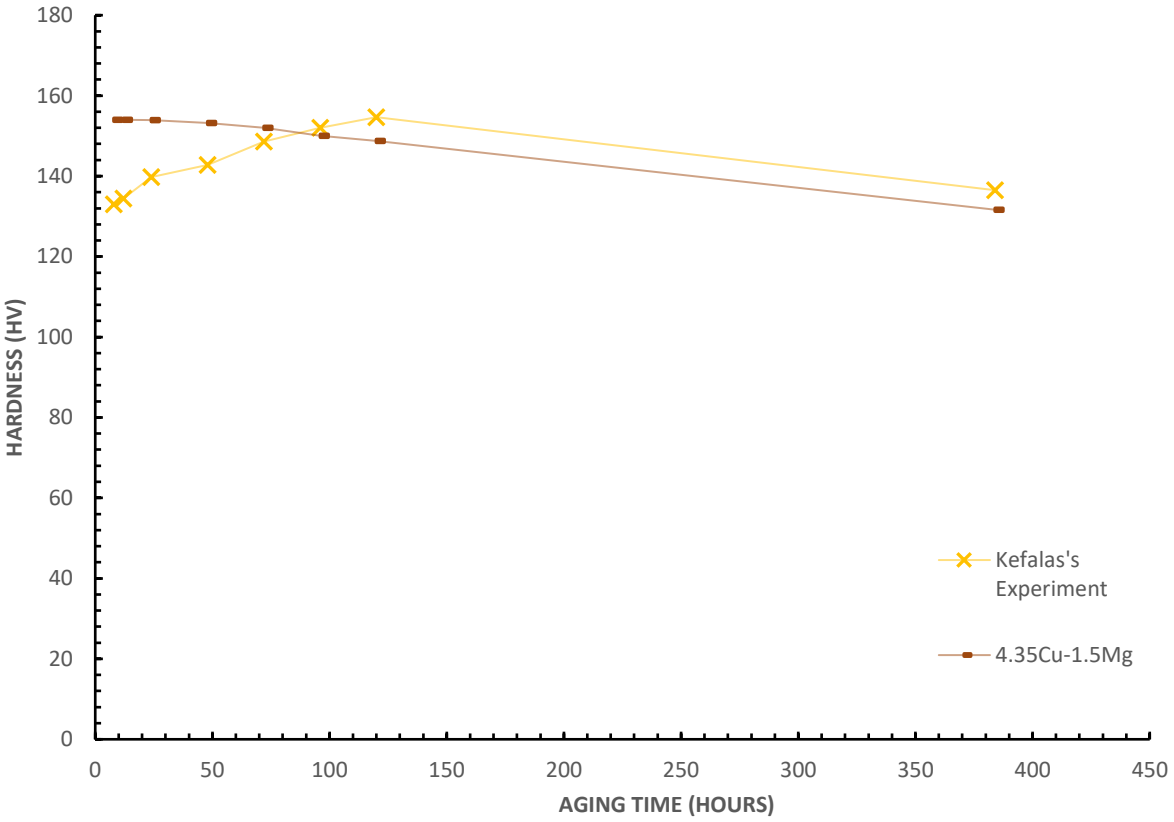

Figure 4-1: Changes in microhardness as a function of aging time during an aging process at 150°C [56].

Moreover, various attempts were made to modify the mobility enhancement prefactor to yield more accurate results. Several perfectors were used, and these attempts are depicted in Figure 4-2. The more accurate attempt was the one with the 0.2 value, which reached the peak hardness between 72-96 hours and remained the same until 120 hours. From that point, coarsening begins but at a slower rate compared to the experimental results.

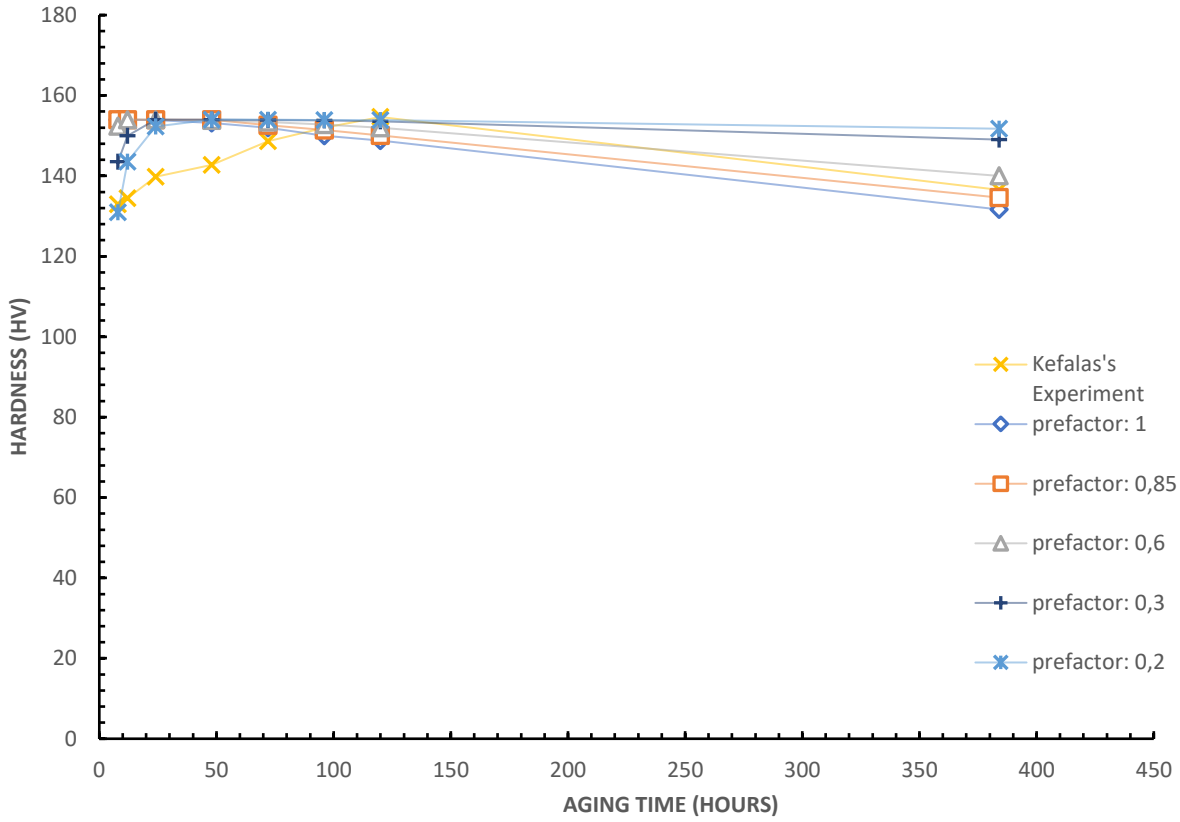

Figure 4-2: Changes in microhardness over time during an aging process at 150°C, for different mobility prefactors [56].

For the 160°C, as illustrated in the following Figure 4-3, the findings are not that accurate in the initial stage of the growth regime. Hardness has reached its maximum value of 157,2 HV in 8 hours compared

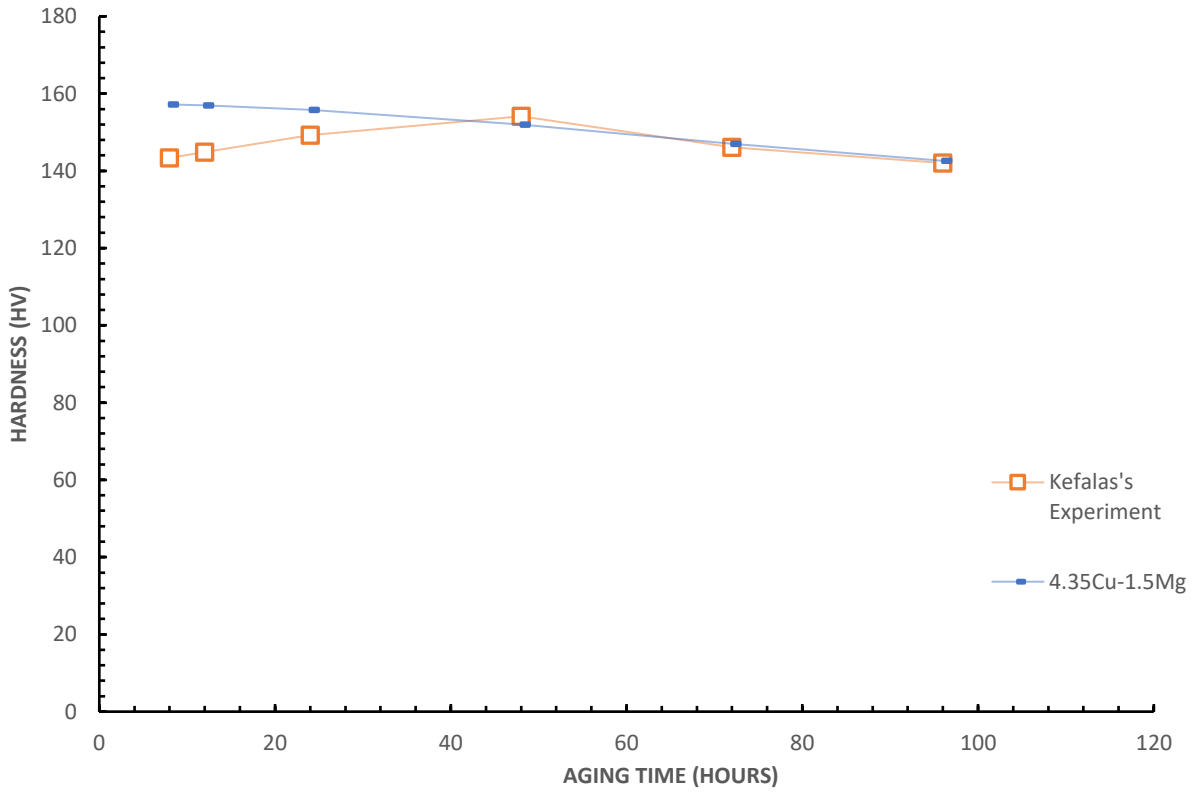

Figure 4-3: Changes in microhardness as a function of aging time during an aging process at 160°C [56].

to the experimental value of 143,4HV at the same time that was measured by Kefalas. Also, in his findings, peak hardness was reached in 48 hours with a value of 154,12 HV. More accuracy is achieved after the 48-hour mark, where the values are almost identical.

As before, there was also an attempt to achieve better results by tampering with the mobility prefactor. These are depicted in Figure 4-4. The prefactors with values of 0.85, 0.6 and 0.3 did not accomplish a better accuracy. On the contrary, the values in the coarsening regime lost accuracy while during the growth regime values stayed nearly the same. The best accuracy in the initial stages of the aging was achieved with a prefactor of 0.1. In this case, the model reached the peak hardness at the same time as the experiment, at 48 hours, at which point coarsening takes place but at a much slower pace.

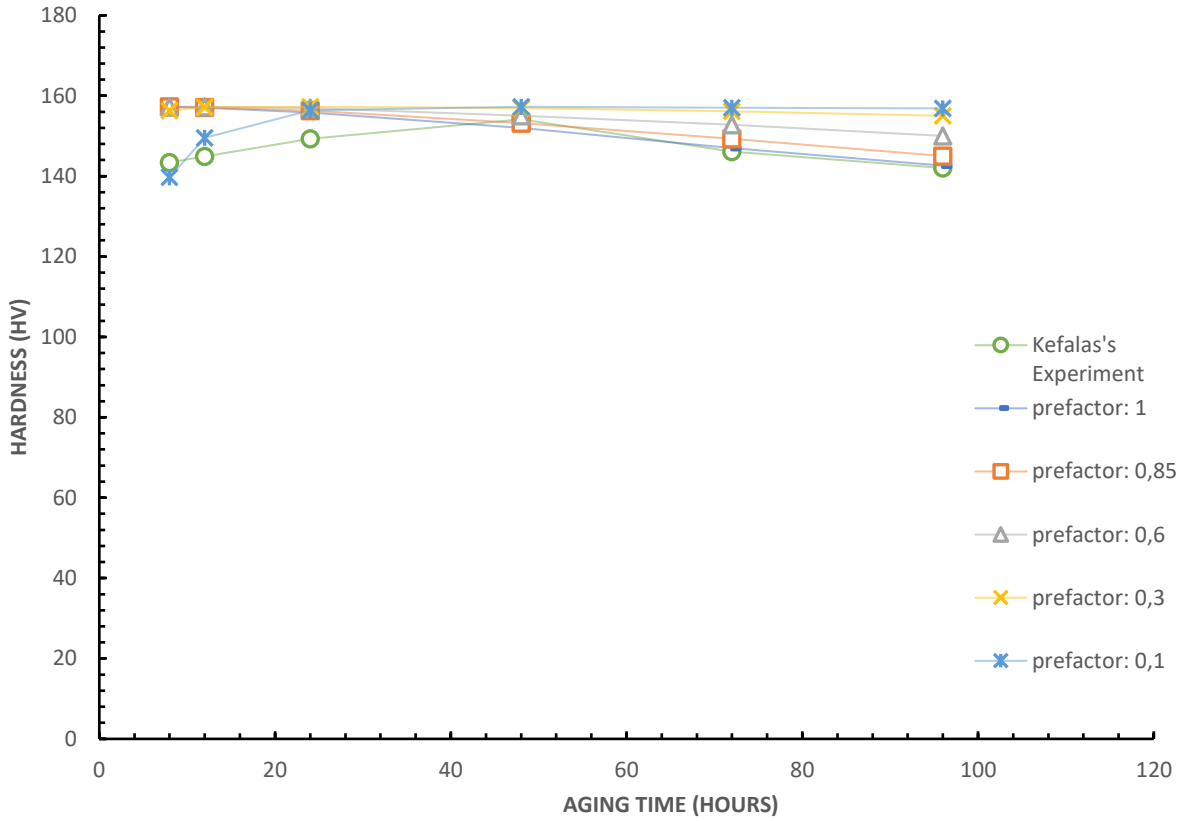

Figure 4-4: Changes in microhardness over time during an aging process at 160°C, for different mobility prefactors [56].

In the case of 170°C, there are experimental values from both Floratos [57] and Karantonidis [58]. The same attempts made earlier for 150°C and 160°C are also applied in this case, but for both experimental procedures.

Firstly, the model results are compared to Floratos findings, as depicted in Figure 4-5. In this case, the maximum hardness is achieved in 15 hours with a value of 128HV which is not in compliance with the experimental findings, where peak hardness is achieved after 48 hours but is not that different from the value of 121HV after 15 hours that was measured by Floratos.

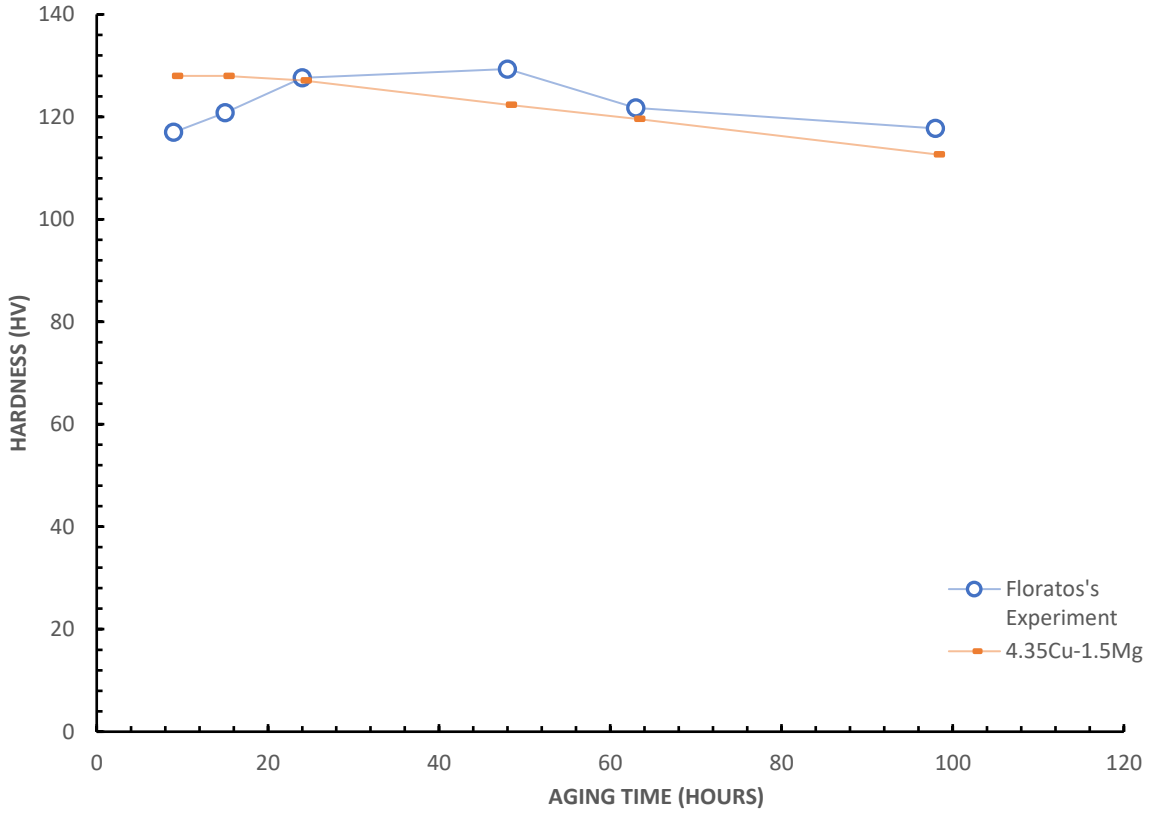

Figure 4-5: Changes in microhardness as a function of aging time during an aging process at 170°C [57].

In the figure below (Figure 4-6), the mobility prefactors used to attain better results are presented. In this case, prefactors with values of 0.1 and 0.05 achieve identical results until the peak hardness is reached but fail to coarsen at the same rate as the experiment. On the other hand, prefactors with values of 0.85 and 0.6 predict the coarsening regime with a very good accuracy.

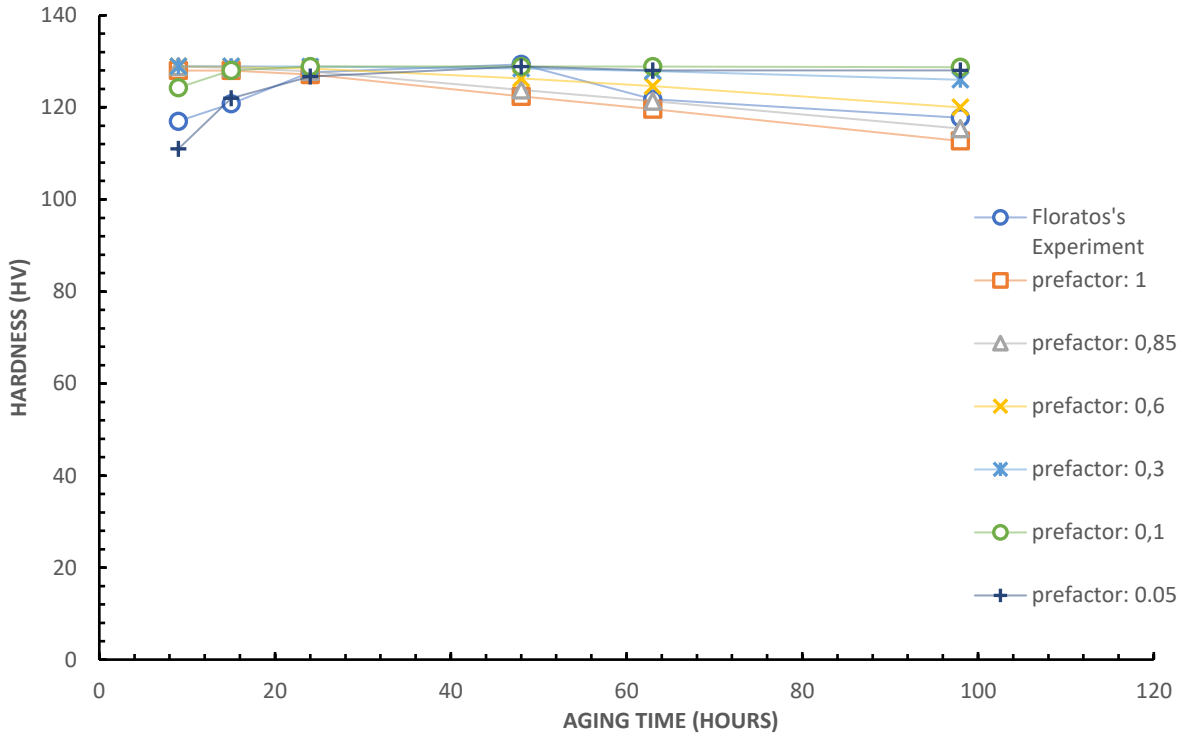

Figure 4-6: Changes in microhardness over time during an aging process at 170°C, for different mobility prefactors [57].

When it comes to Karantonidis work, the results derived from the model are compared to his findings, in Figure 4-7. In this case, the model results achieve a very high accuracy with the experiment. In both cases, the peak hardness is achieved in 6 hours with the model predicting a value of 128.93HV while Karantonidis measured a value of 132,61HV.

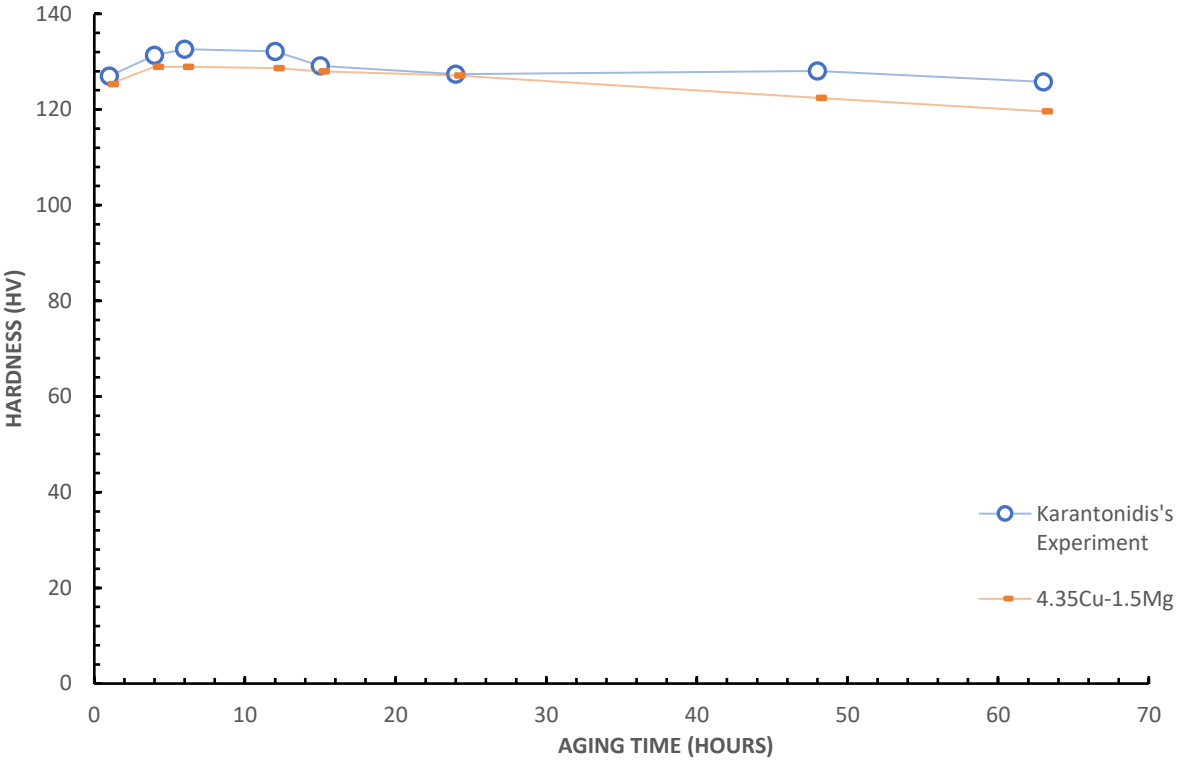

Figure 4-7: Changes in microhardness as a function of aging time during an aging process at 170°C [58].

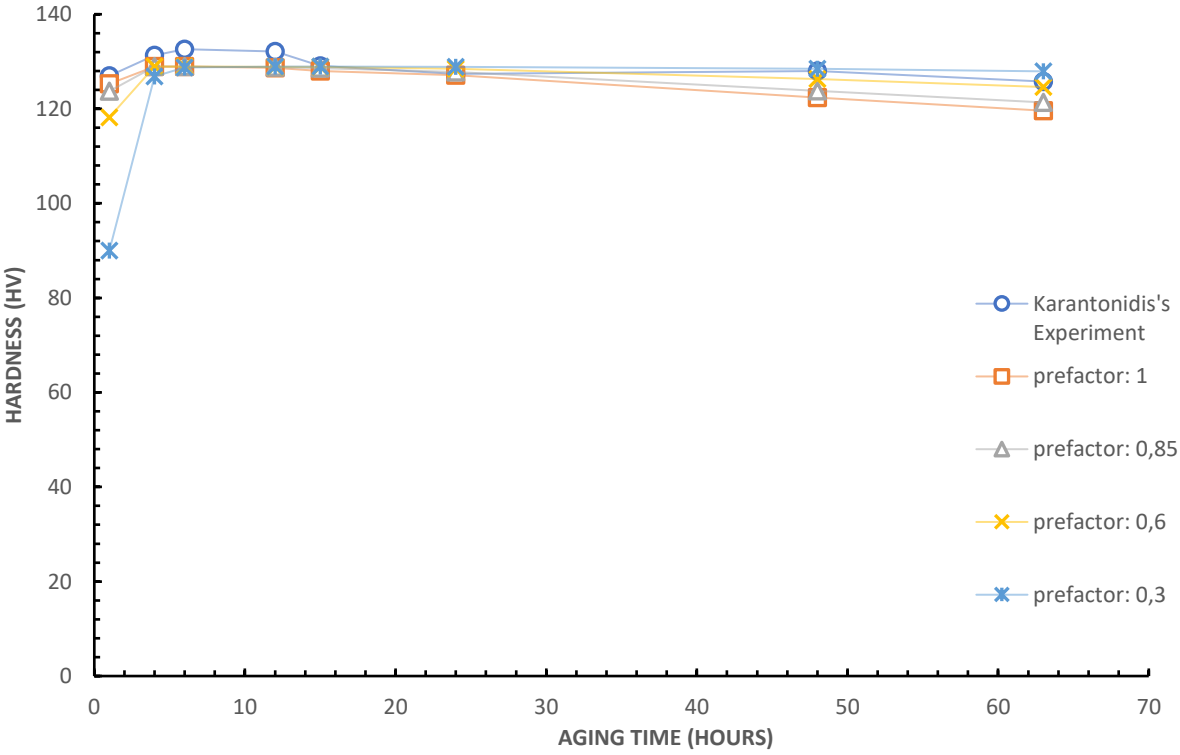

Figure 4-8: Changes in microhardness over time during an aging process at 170°C, for different mobility prefactors [58].

As earlier, different mobility prefactors were used in this case too and are shown in the above figure (Figure 4-8). As it can be seen, accuracy is maintained in the case of 0.85 and 0.6 prefactors, while the one with a value of 0.3 predicts a value of 90HV in 1 hour which is significantly lower than the measured value of 126.96HV.

In the case of 210°C, as previously, model predictions and experimental results are portrayed in Figure 4-9. In both cases, peak hardness is achieved in 1 hour and are identical, 125.64HV in Karantonidis work versus 124HV in this work. What can be noticed is that after 15 hours into aging, the model predicts significantly lower hardness compared to the experimental values. In Figure 4-10, the same model, with different mobility prefactors, is presented. Overall, prefactors of 0.6 and 0.3 are the ones that improve the accuracy, with the latter matching the experimental measures in every point. The 0.85 prefactor seems to induce only a marginal improvement, but it's a step in the right direction.

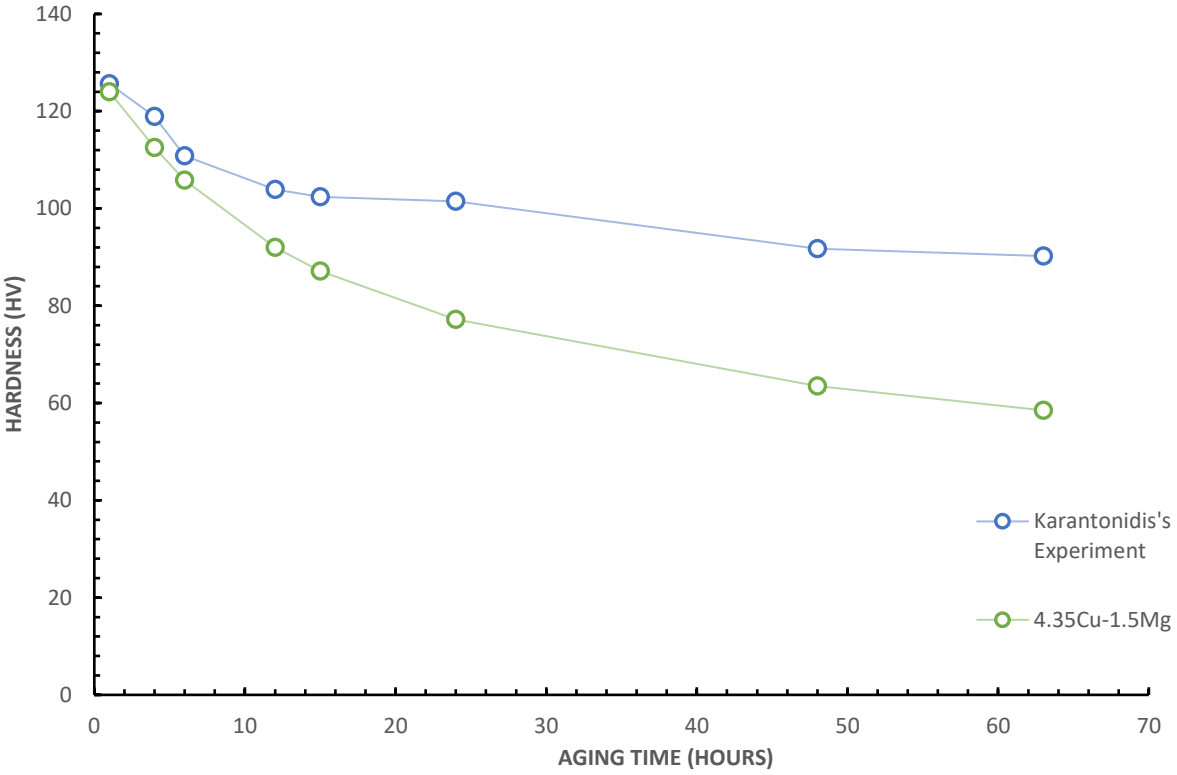

Figure 4-9: Changes in microhardness as a function of aging time during an aging process at 210°C [58].

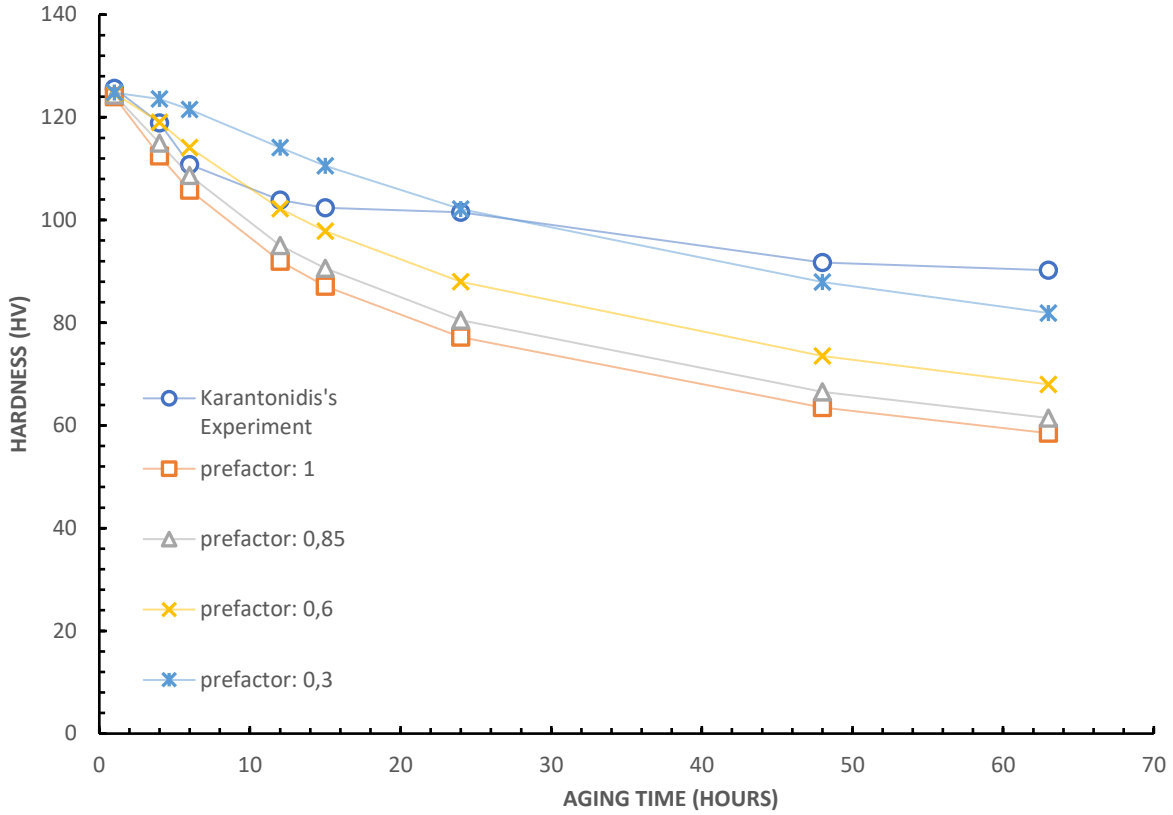

Figure 4-10: Changes in microhardness over time during an aging process at 210°C, for different mobility prefactors [58].

4.2 Hardness evolution for different compositions

The subsequent figures illustrate the outcomes of the different compositions that were applied to observe the changes in hardness as a result of aging at 2 different temperatures, 170°C and 210°C. The level of solid solution supersaturation rises with higher concentrations of alloying elements in the system. Consequently, an elevation in the composition of any of the alloying elements can amplify peak hardness by accelerating nucleation and growth rates, as illustrated in the following figures. Nevertheless, the time necessary to achieve peak hardness remains constant, as indicated by the findings. The extent to which the addition of an alloying element can enhance peak hardness varies depending on the specific element and will be discussed further for each case.

4.2.1 Model based on S-phase spherical precipitates

4.2.1.1 Precipitation results and various alloy compositions in 170°C

For the 170°C, the different response in hardening is presented in the following figures. In each case, the concentrations are kept the same as the AA2024 and only the concentration of one element is tested for various compositions. Moreover, the results are compared for both Floratos and Karantonidis findings.

For various copper compositions and for the case of Floratos findings, the age hardening response is presented in Figure 4-11. As mentioned earlier, the higher the composition of copper the higher the peak hardness. For the 4.9% copper composition, the hardness reaches its highest value of 142HV while for the 4% composition the hardness reaches the maximum value of 119,67HV. The most accurate composition is the one of 4.5% and with some modifications in the mobility prefactor will become even more precise. The same conclusions can be, also, made for Karantonidis findings and are illustrated in Figure 4-12. Peak hardness is reached with the 4.9% copper concentration and has a value of 142.86HV in between 4-6 hours. This confirms the argument made earlier. Additionally, in this case the 4.5% copper concentration seems to exhibit the highest accuracy.

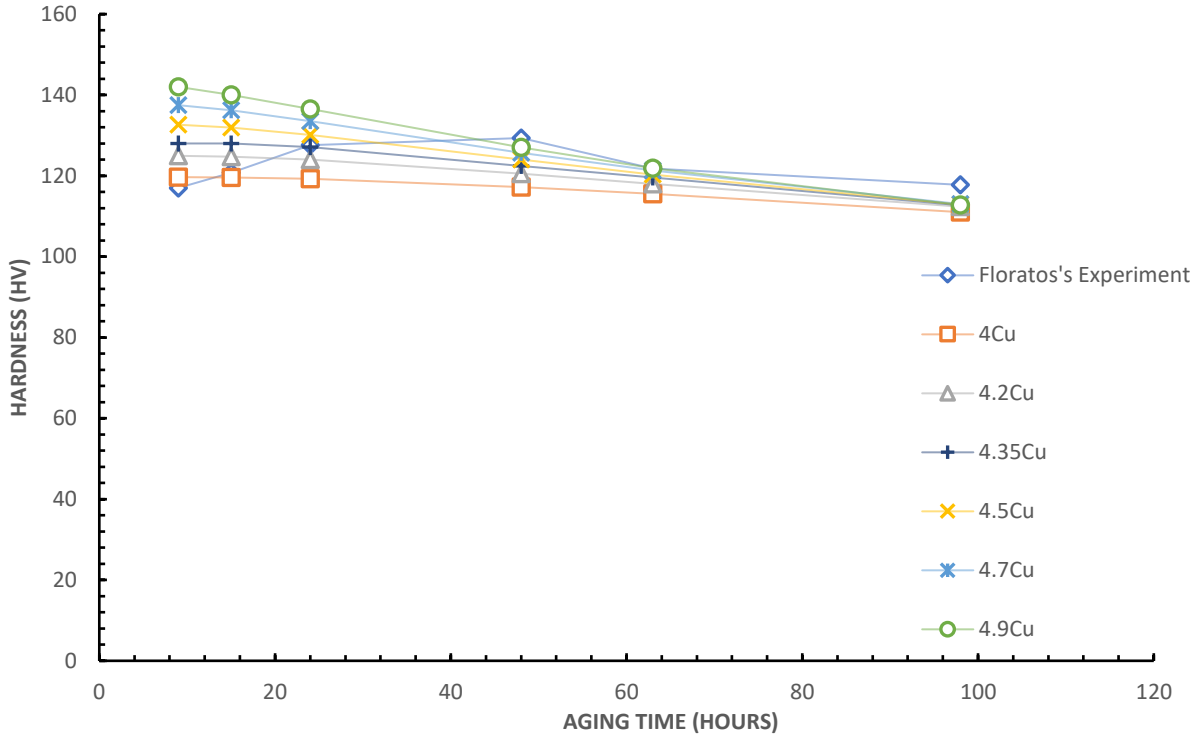

Figure 4-11: Hardness evolution as a function of aging time across different copper concentrations compared to Floratos's experiment, at 170°C [57].

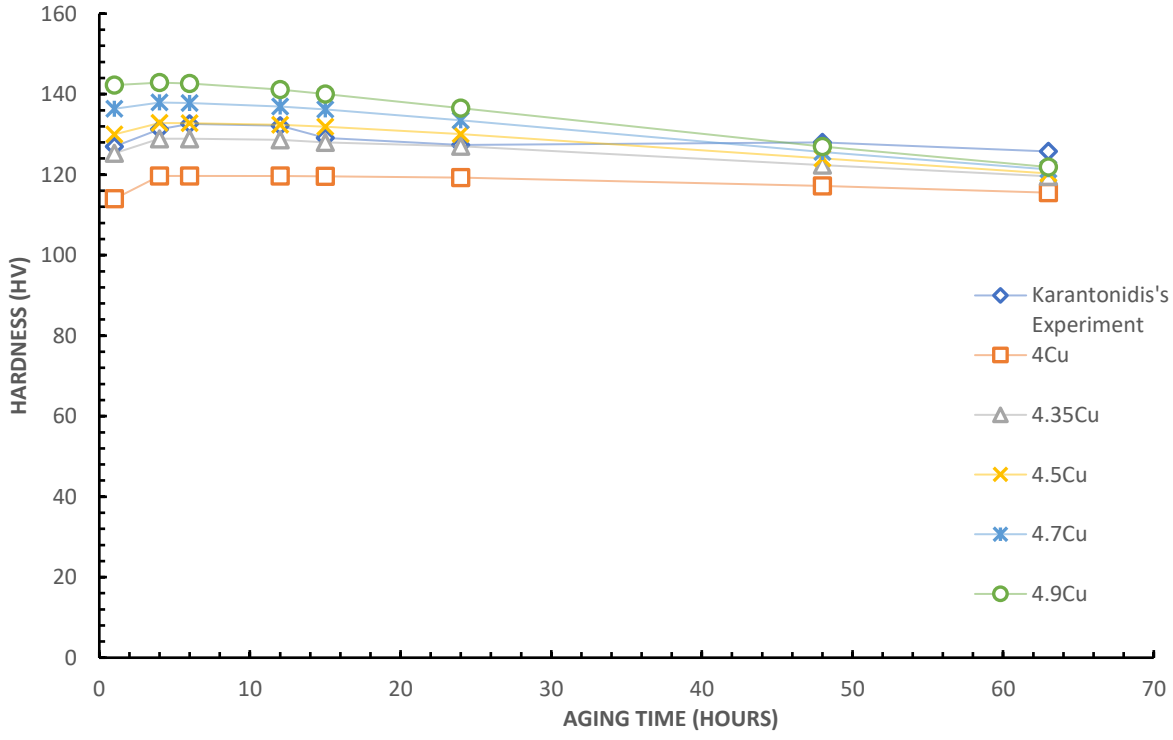

Figure 4-12: Hardness evolution as a function of aging time across different copper concentrations compared to Karantonidis's experiment, at 170°C [58].

For the various magnesium compositions, the model results are presented in Figures 4-13, 4-14. Firstly, comparisons are made with Floratos data and then with Karantonidis ones. Magnesium exhibits the exact same behavior as copper. The higher its concentration, the higher the peak hardness achieved. Furthermore, the alloy with 1.8% magnesium composition achieved a peak hardness of 149.75HV in 9-15 hours. This value proves that magnesium addition achieves a higher hardness than that of any copper addition. The alloys with 1.4% and 1.6% achieve really good accuracy with the experimental data. When the model data are compared to Karantonidis, the exact same behavior is noticed. The peak hardness here is achieved in 6 hours on every occasion. The alloy with 1.8% magnesium achieves the highest peak hardness with a value of 149.85HV and the one with 1.3% the lowest one, 114.28HV. In this case, the 1.6% composition achieves nearly absolute accuracy across all time intervals, with the 1.4% alloy achieving good accuracy.

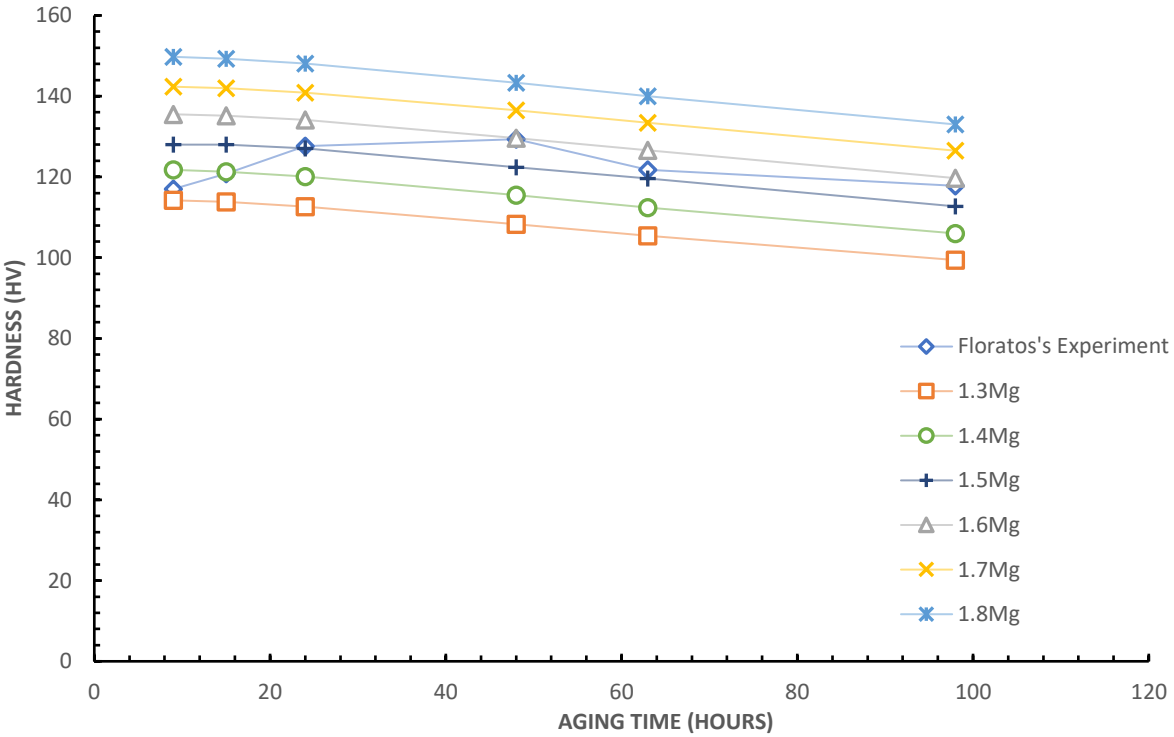

Figure 4-13: Hardness evolution as a function of aging time across different magnesium concentrations compared to Floratos's experiment, at 170°C [57].

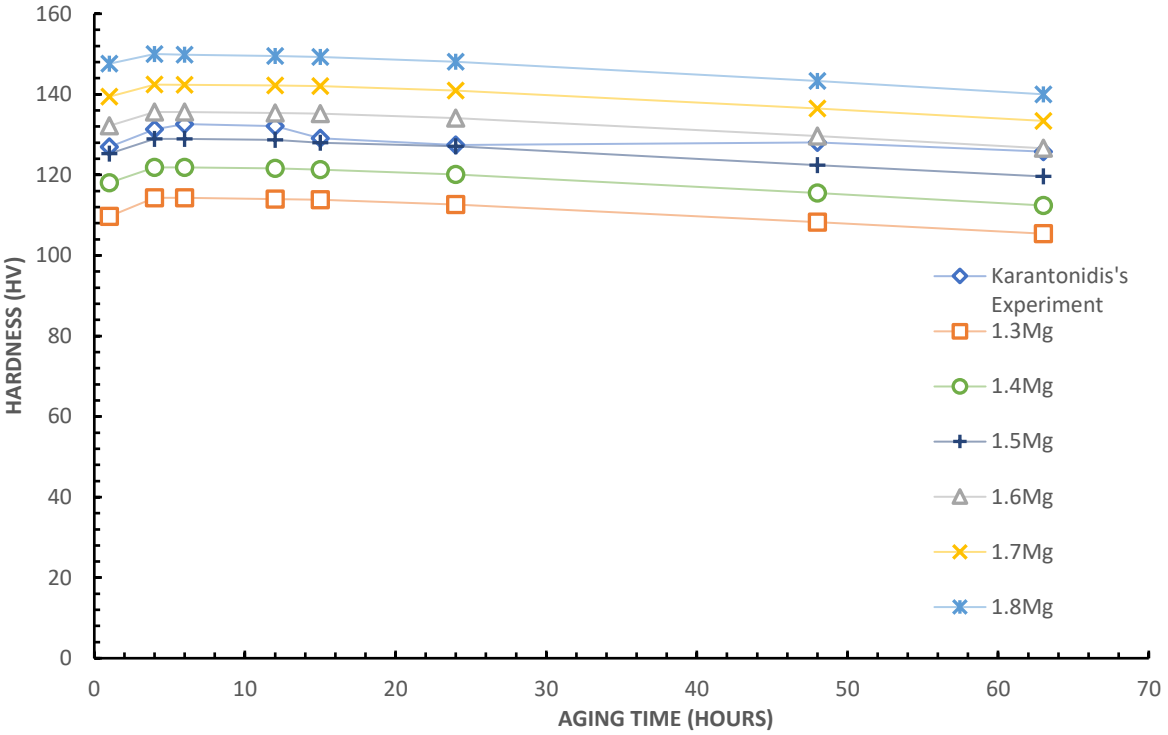

Figure 4-14: Hardness evolution as a function of aging time across different magnesium concentrations compared to Karantonidis's experiment, at 170°C [58].

After numerous trials, involving different alloy compositions, to approach the experimental findings of Floratos and Karantonidis, the Al-4.4Cu-1.5Mg alloy with a mobility prefactor of 0.1 and the Al-4.35Cu-1.5Mg alloy with a mobility prefactor of 0.6 were selected as the best approximations, respectively. In the first case, peak hardness is 130.25HV which is almost equal to the experimental value of 129.34HV. Both values are reached in 48 hours. The second alloy mentioned above, matched the experimental value of 132HV and was reached in 6 hours in both scenarios.

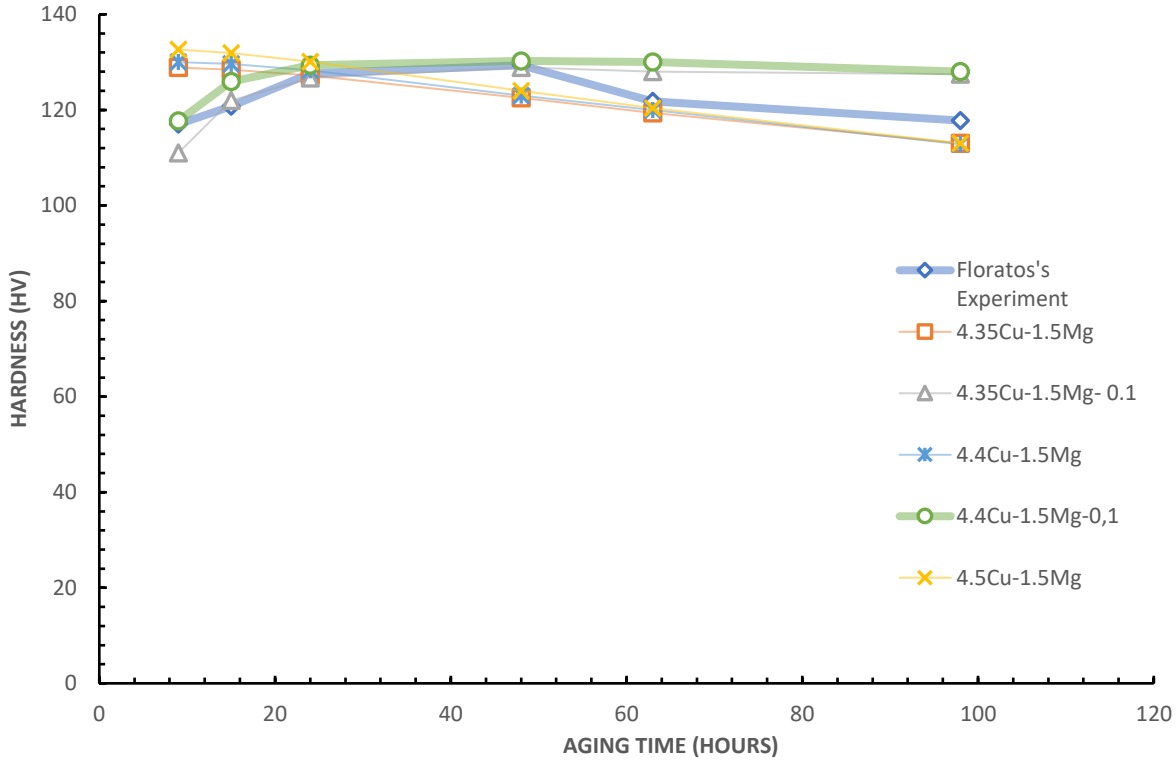

Figure 4-15: Various alloy compositions, with the alloy Al-4.4Cu-1.5Mg with a mobility prefactor of 0.1 being the best approximation to Floratos's findings at 170°C.

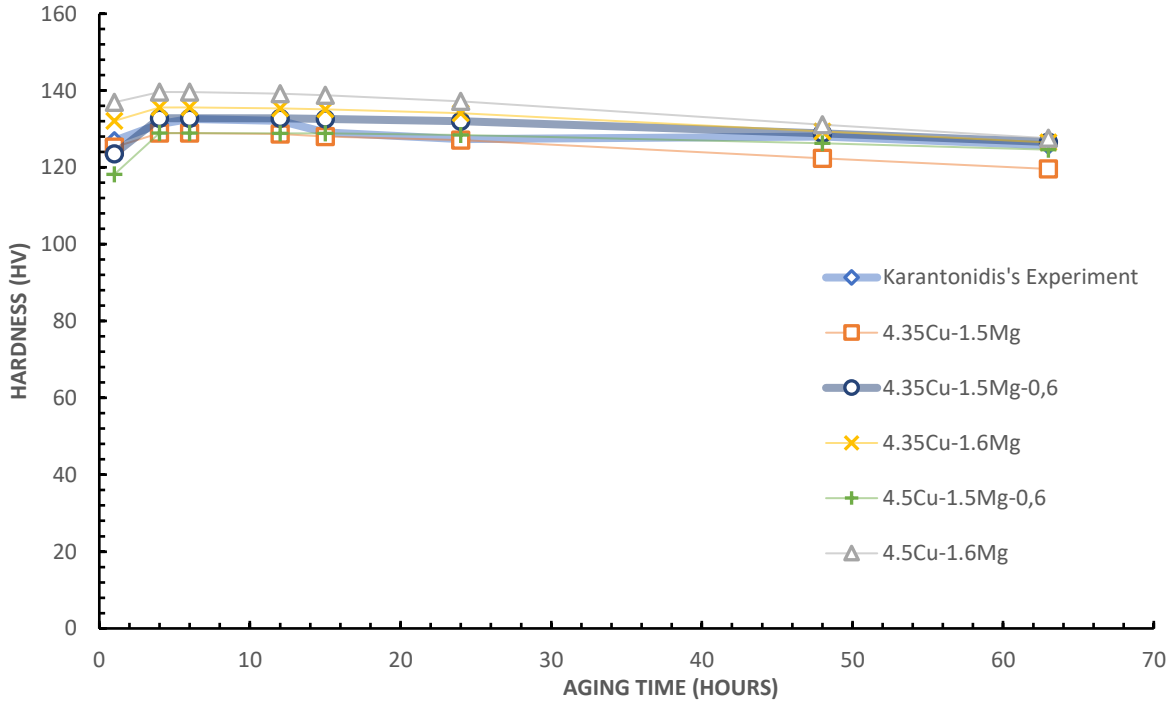

Figure 4-16: Various alloy compositions, with the alloy Al-4.35Cu-1.5Mg with a mobility prefactor of 0.6 being the best approximation to Karantonidis's findings at 170°C.

4.2.1.2 Precipitation results and various alloy compositions in 210°C

When it comes to the precipitation modeling in 210°C, the results are depicted in the following figures, Figure 4-15, Figure 4-16. Firstly, the various copper compositions are presented, from 4.2% to 4.9%. All variations behave in the same way, exhibiting their peak hardness in 1 hour. As it can be noticed, the maximum hardness increases as the composition in copper increases which confirms earlier observations in 170°C. The alloy with 4.9% composition has a peak hardness of 137HV in 1 hour while the one with 4.2% copper has a maximum hardness of 120HV. After 6 hours, the model loses hardness with a higher rate compared to the experiment. From that point, all compositions perform in the same way.

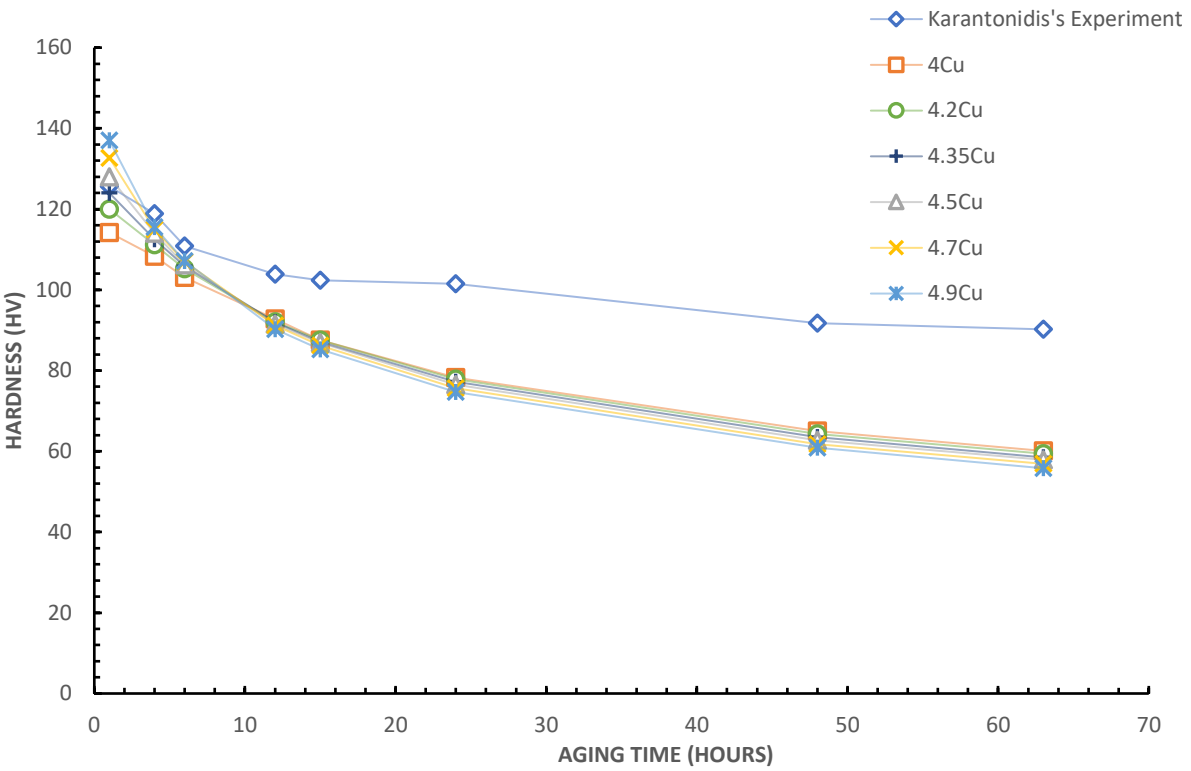

Figure 4-17 Hardness evolution as a function of aging time across different copper concentrations compared to Karantonidis's experiment, at 210°C [58].

Magnesium variations are portrayed in Figure 4-16 below. An immediate observation is that the information previously stated about magnesium at 170°C holds equally true in this instance. The higher peak hardness is noticed in 1.8% magnesium concentration and has a value of 148.63HV in 1 hour. Another observation that can be made is that as the magnesium concentration increases, the alloy coarsens at a slower rate. For example, after 63 hours, the hardness of the 1.8% magnesium alloy is 67.75HV versus the 52.35HV of the one that has 1.3% magnesium.

In this case, also, there was an effort to approach the peak hardness by applying different compositions. The alloy Al-4.35Cu-1.5Mg with a mobility prefactor of 0.3 approached the findings of Karantonidis with excellent accuracy. Peak hardness was 124.74HV in the model while in the experiment was found equal to 125.64. In both scenarios, it was reached in 1 hour.

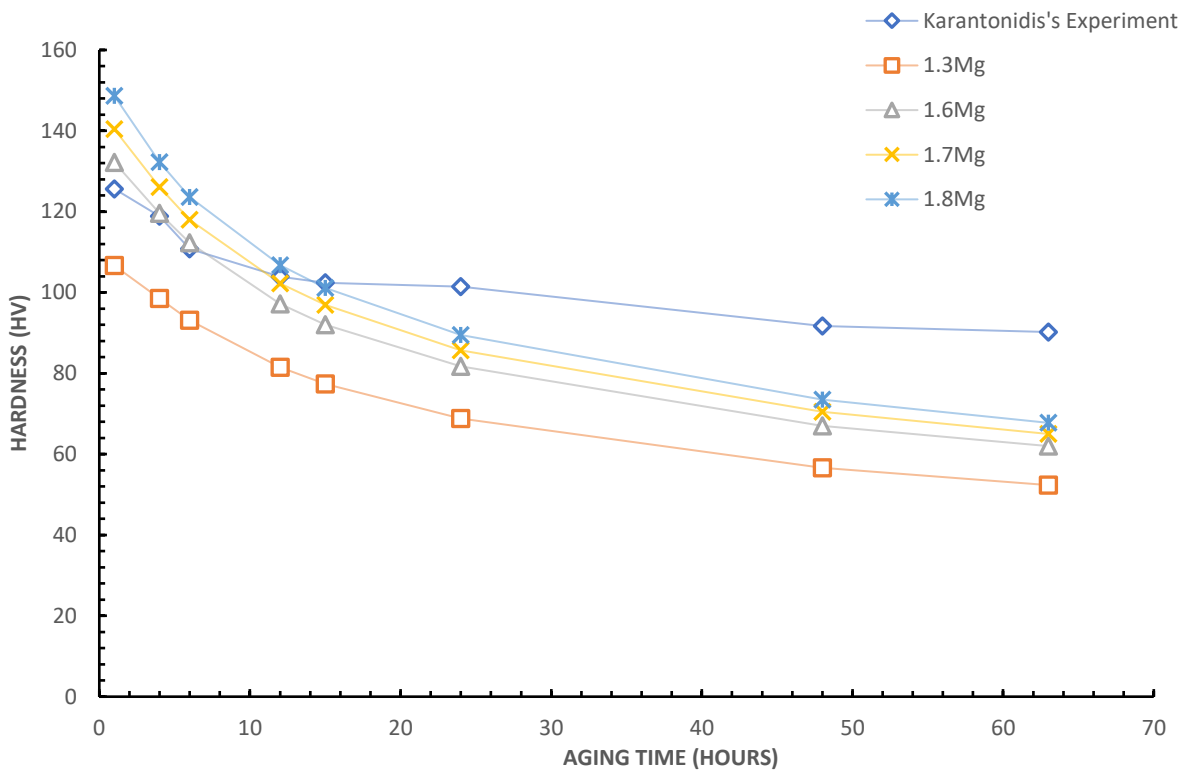

Figure 4-18: Hardness evolution as a function of aging time across different magnesium concentrations compared to Karantonidis's experiment, at 210°C [58].

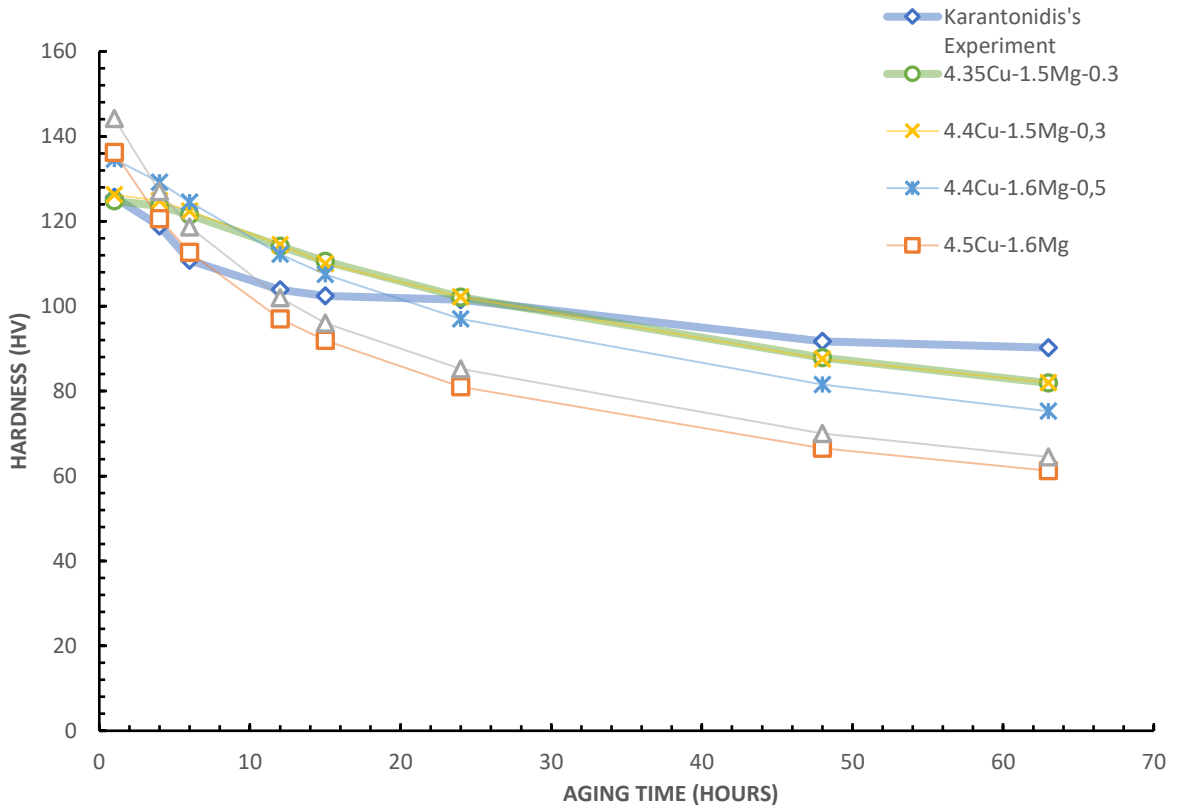

Figure 4-19: Various alloy compositions, with the alloy Al-4.35Cu-1.5Mg with a mobility prefactor of 0.3 being the best approximation to Karantonidis's findings at 210°C.

4.2.2 Model based on S'-phase, S-phase and needle morphology precipitates

As mentioned earlier in Chapter 3, S' phase and its equilibrium variant, S-phase, are indistinguishable [3,8,23,25,34,35,38]. However, there was an effort to calculate the possible contributions in the total hardness of the material. The first obstacle was that there is no available value for the interfacial energy of the S' phase in the bibliography. On that note, there were two attempts where in each trial only one of these two phases was assumed the precipitating phase. The settings of TC-PRISMA were kept default, except for the morphology of the precipitating phase which was assumed to be needle-shaped with an aspect ratio of 10 [8,25]. The results were identical and are depicted in Figure 4-20.

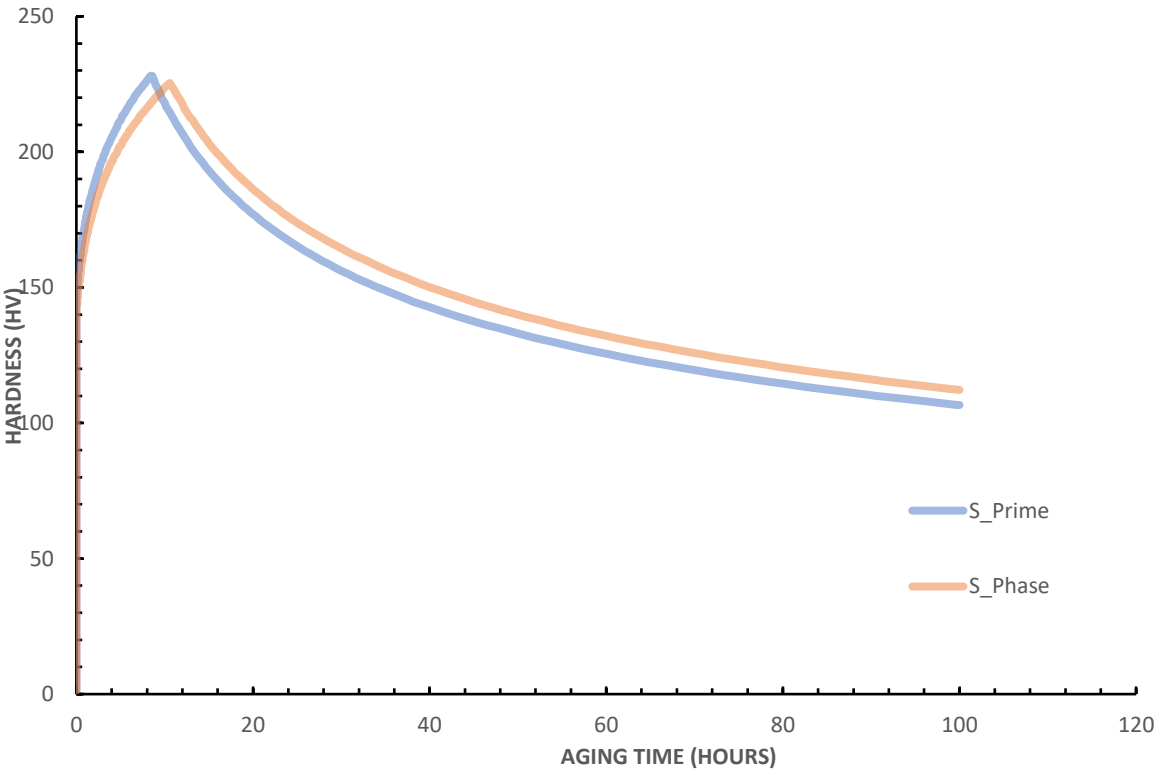

Figure 4-20: Hardness evolution of S-Prime and S-Phase in default settings and needle morphology, in 170°C.

The precipitation module was applied similarly to different alloy compositions and enhancing mobility prefactors, but this time with needle shaped precipitates with an aspect ratio of 10. This approach was then utilized to the one-step aging at 170°C and 210°C with the assumption of one hardening phase, the S phase. The most accurate estimation was obtained for the Al-4.35Cu-1.5Mg alloy but with different prefactors. More specifically, for the case of Floratos at 170°C a prefactor of 0.05 was selected while at the same temperature a prefactor of 0.2 led to a very good approximation of Karantonidis experimental measurements. At 210°C, a prefactor of 0.1 was selected. The hardness curves of each case are presented in the following figures.

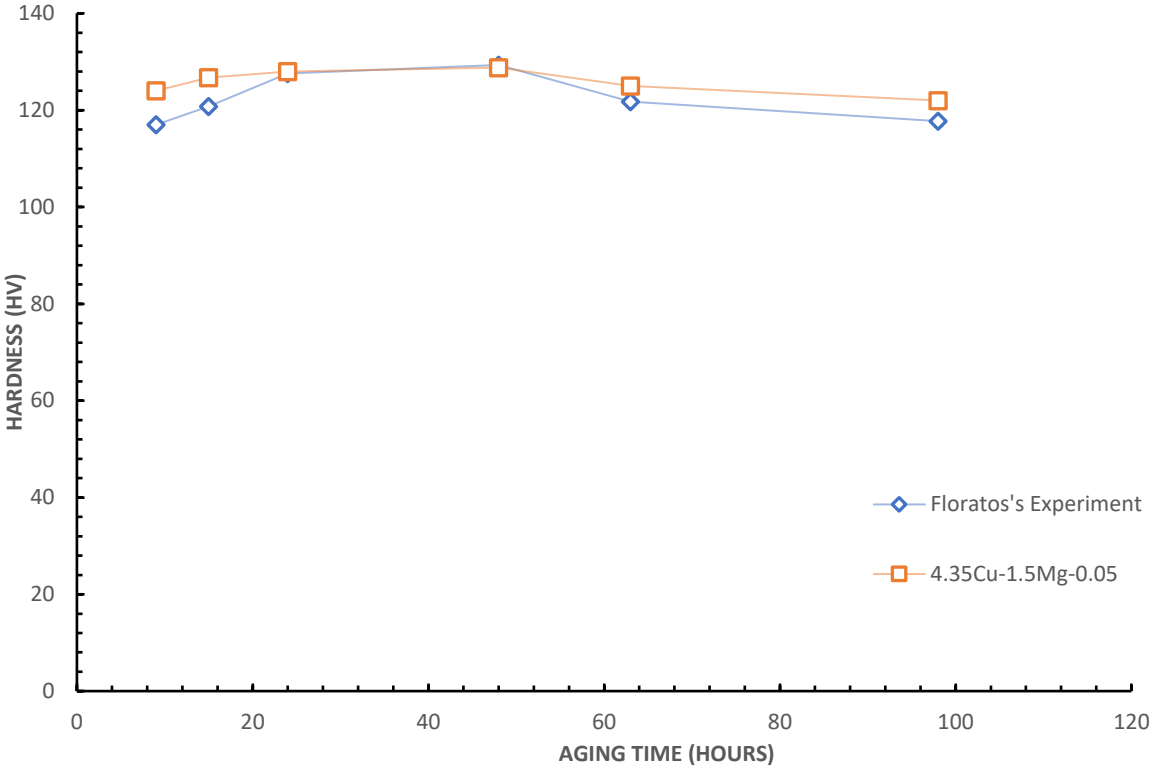

Figure 4-21: Changes in microhardness as a function of time during an aging process at 170°C for needle shaped precipitates compared to Floratos's experiment.

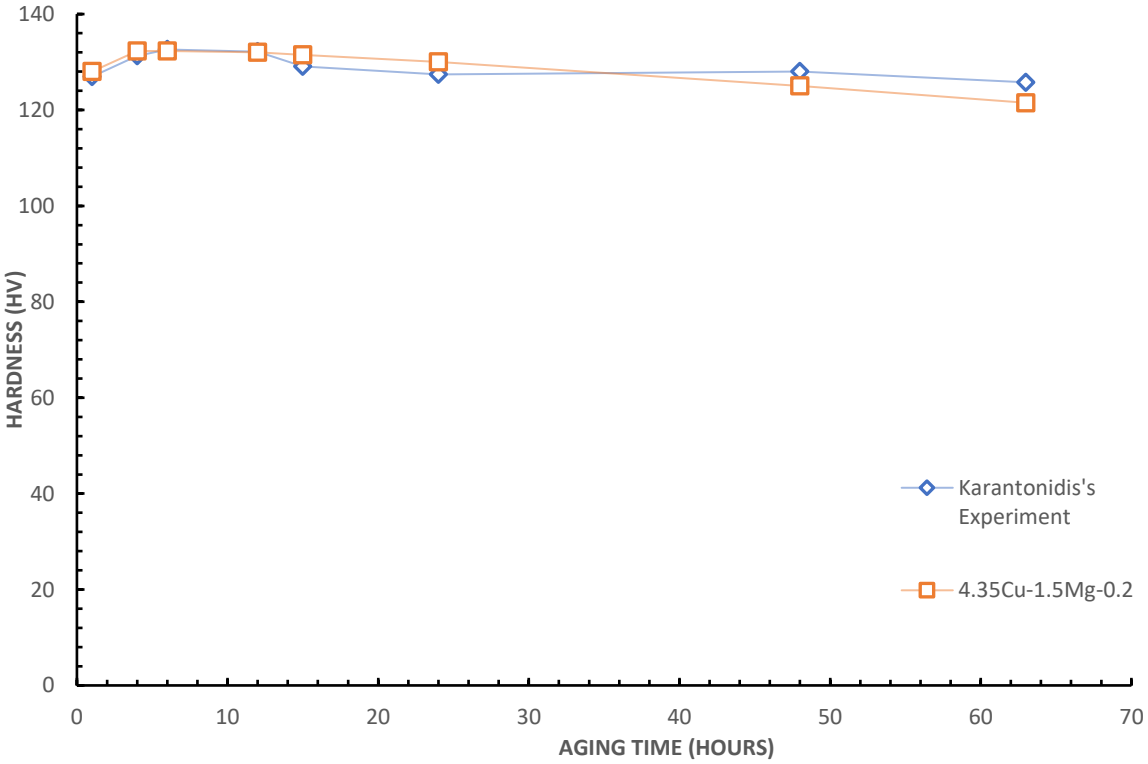

Figure 4-22: Changes in microhardness as a function of time during an aging process at 170°C for needle shaped precipitates compared to Karantonidis's experiment.

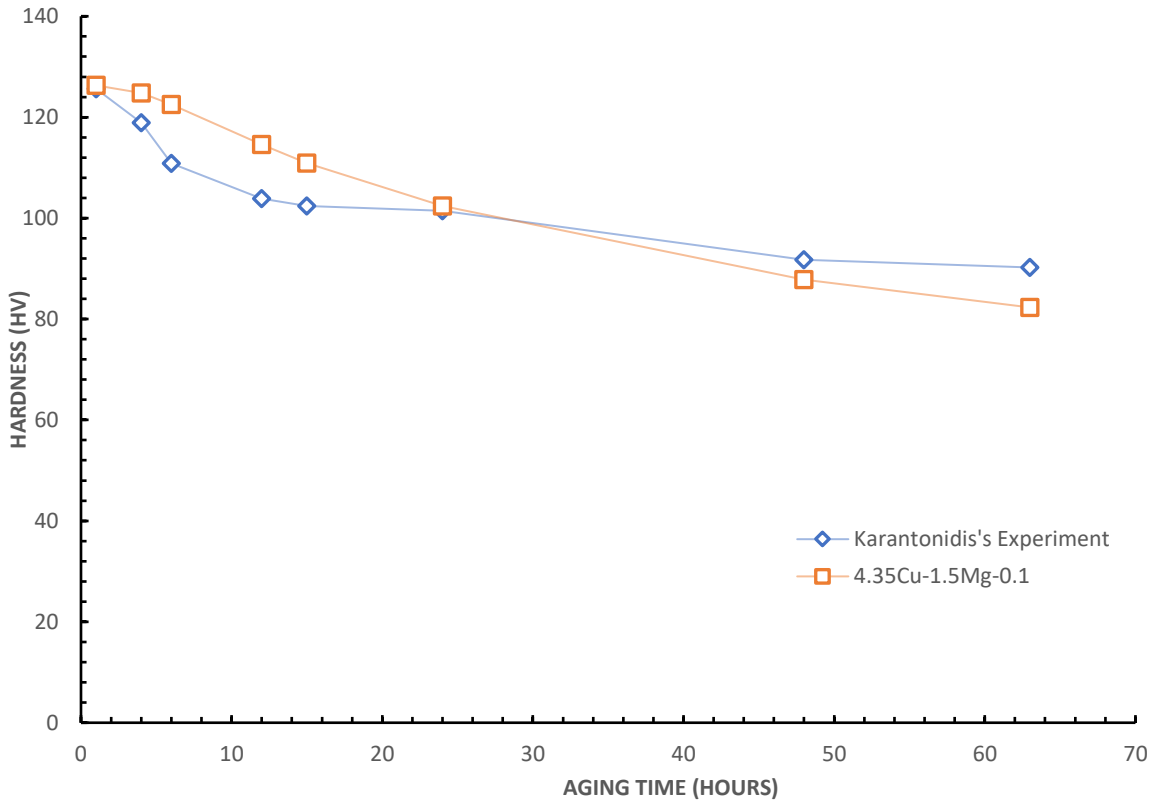

Figure 4-23: Changes in microhardness as a function of time during an aging process at 210°C for needle shaped precipitates compared to Karantonidis's experiment.

In case of Floratos, peak hardness is achieved after 48 hours in the model which agrees with his findings and has a value of 128.8HV. Overall, the approximation is very accurate in every time interval of the experiment. When it comes to Karantonidis and for the 170°C, peak hardness is achieved in 4-6 hours in the model and has a value of 132.3HV while Karantonidis found out 132.61HV. At 210°C, the results become less accurate but overall agree with the experiment. Both have similar values at the beginning of the aging process (125.64HV versus 126.3HV) while, until the 24 hour interval, the model deviates by a small margin from the experimental findings. From that point and on, till the end of the experiment, the results agree again with pretty good accuracy.

4.2.2.1 Changes in distinct properties over the course of aging

In the following diagrams, the effect of different mobility factors over the nucleation rate is depicted for the temperatures of 170°C and 210°C. In both cases, the higher the nucleation rate the faster it reduces. Decreasing the mobility prefactor extends the duration of nucleation while resulting in lower nucleation rates during the initial stages, as is depicted in Figure 4-24 and Figure 4-25. Another comment that can be made is that higher temperature leads to higher nucleation rates. For the same material and mobility prefactor of 1, at 170°C the nucleation rate is in the magnitude of 10^{21} $m^{-3}s^{-1}$ while at 210°C it's in the magnitude of 10^{22} $m^{-3}s^{-1}$.

In Figures 4-26, 4-27 and 4-28, the progression of nucleation rate, precipitate number density, and normalized nucleation driving force for the S-phase is depicted, along with their interrelationships. At the onset of precipitation, the nucleation rate and the driving force achieve their anticipated peak values. As nucleation concludes, meaning the nucleation rate reaches zero, the precipitate's number density, indicating the quantity of particles per volume unit, reaches its zenith. Throughout the growth phase, this number density steadily decreases, likely due to the dissolution of certain particles.

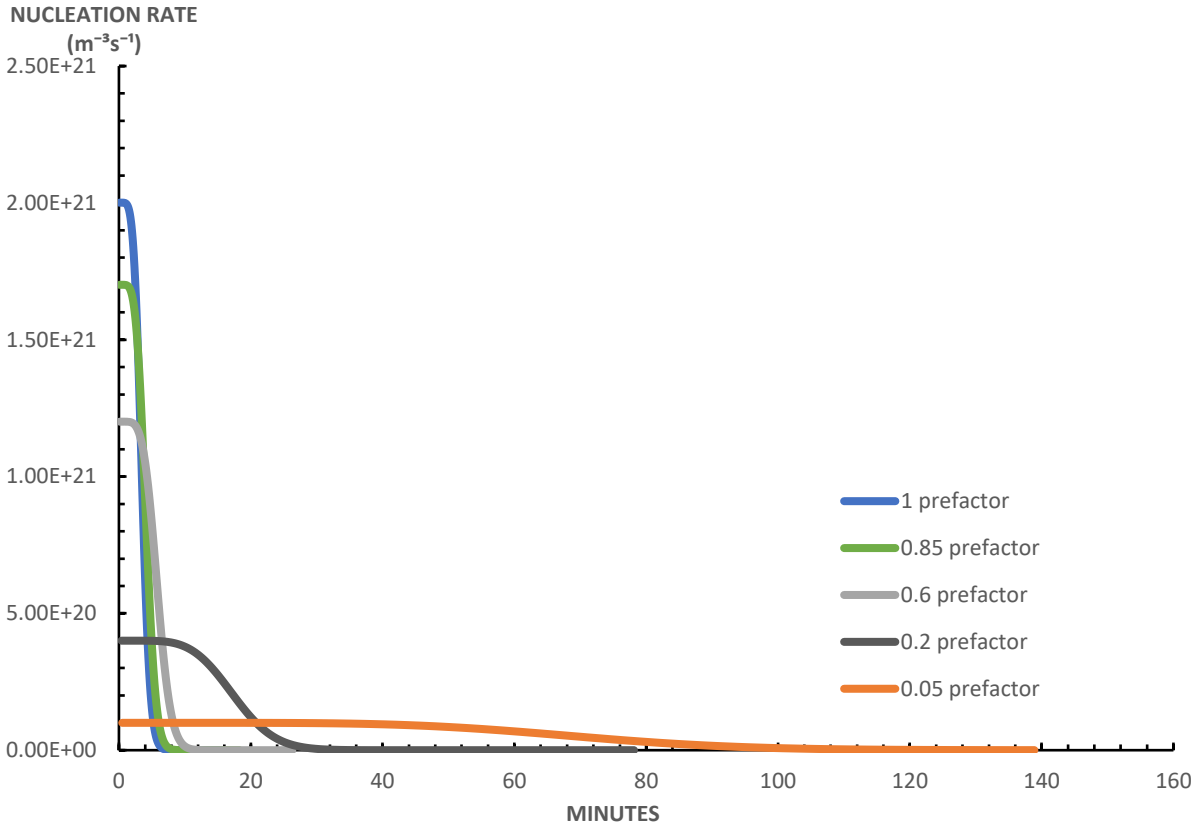

Figure 4-24: Nucleation rates for different mobility prefactors for the Al-4.35Cu-1.5Mg alloy, at 170°C.

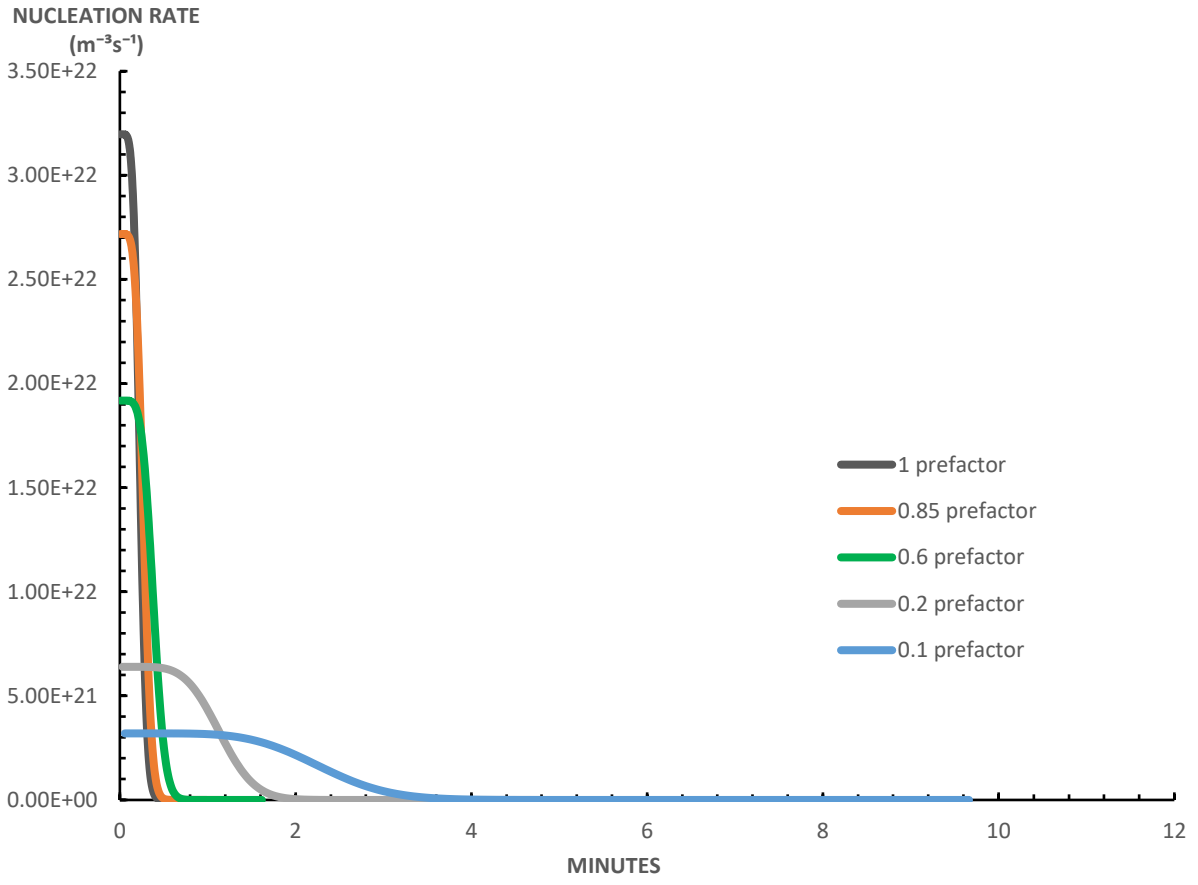

Figure 4-25: Nucleation rates for different mobility prefactors for the Al-4.35Cu-1.5Mg alloy, at 210°C.

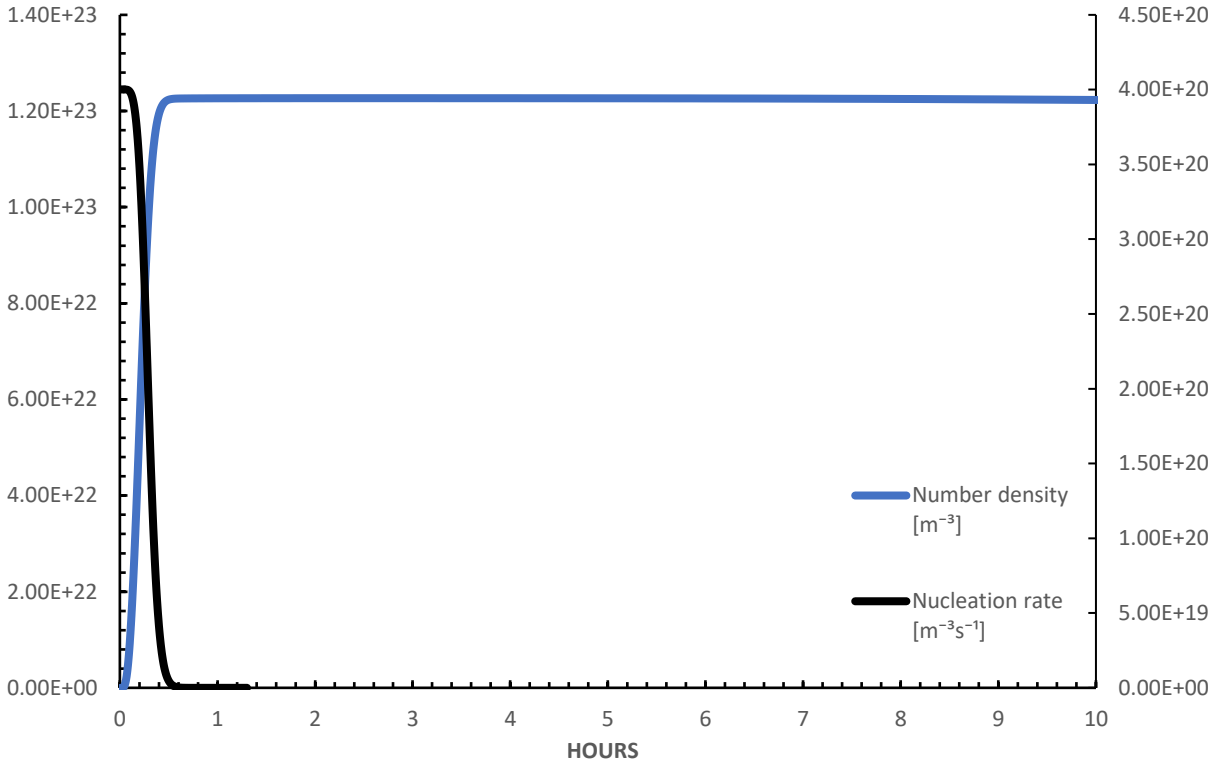

Figure 4-27: Evolution of number density and nucleation rate in the aging process of 170°C, in the Al-4.35Cu-1.5Mg alloy with a mobility prefactor of 0.2.

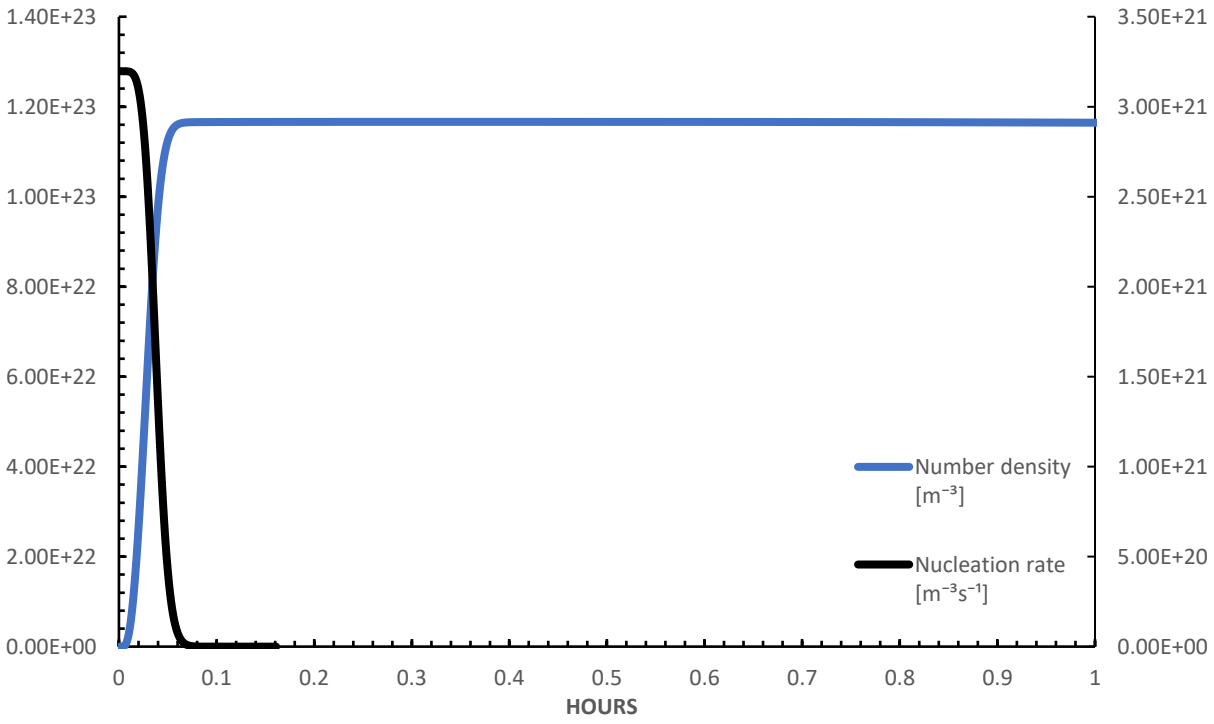

Figure 4-26: Evolution of number density and nucleation rate in the aging process of 210°C, in the Al-4.35Cu-1.5Mg alloy with a mobility prefactor of 0.1.

The driving force experiences a swift decline during nucleation and the initial phases of growth, owing to the decrease in solid solution supersaturation. Following this, the driving force continues to diminish, albeit at an exceedingly slow pace. While the driving force for nucleation remains active throughout the 100-hour aging period, nucleation ceases once the driving force descends below the energy barrier required for nucleation.

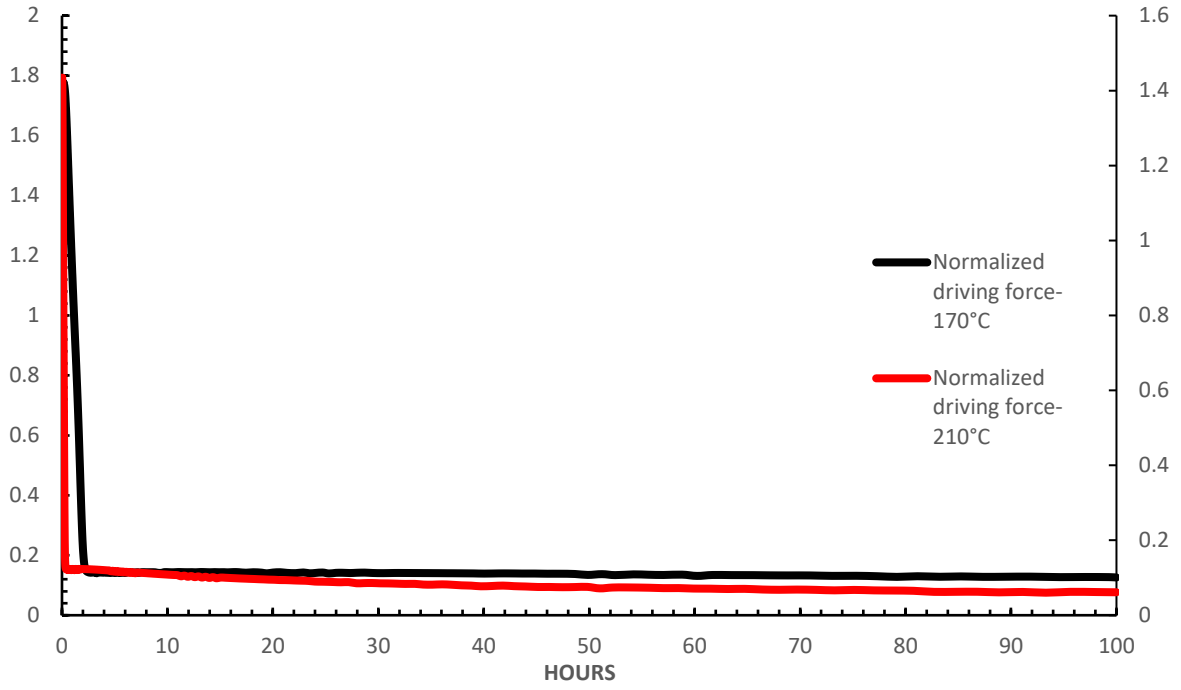

Figure 4-28: Evolution of the normalized driving force during aging at 170°C and 210°C.

At the initiation of nucleation, the S phase experiences an abrupt rise in volume fraction, reaching a value of 0.06593 at 170°C and 0.06565 at 210°C, as depicted in Figure 4.29 and Figure 4.30. This increment persists, albeit at a gradual pace. Despite the diminishing number density of precipitates, the volume fraction continues its ascent until the treatment's conclusion due to particle growth and coarsening. At the point of maximum hardness, the volume fraction equals 0.067 at 170°C and 0.06566 at 210°C, while the number density stands at 1.2262×10^{23} and 1.16423×10^{23} particles per cubic meter, respectively.

Figure 4.31 and Figure 4.32 display the size distributions of both the radius and length of precipitates at the hardness peak for 170°C and 210°C. In 170°C, the predominant form among these needle-shaped precipitates, 5.94×10^{31}, exhibits dimensions of 45.9nm in length and 4.94nm in radius while in 210°C, 3.34×10^{31} of the precipitates have dimensions 55.67nm in length and 6nm in radius.

Figure 4.33 outlines the evolution of S phase precipitate composition over aging time in the Al-4.35Zn-1.5Mg alloy, for both 170°C and 210°C. The mass percentages of aluminum, copper and magnesium exhibit a nearly constant trend, with values of 38.05 and 44.81 and 17.14, respectively. At peak hardness, the composition in mass percent of the S phase precipitates is (38.05)Al(17.14)Mg(44.81)Cu, according to the results.

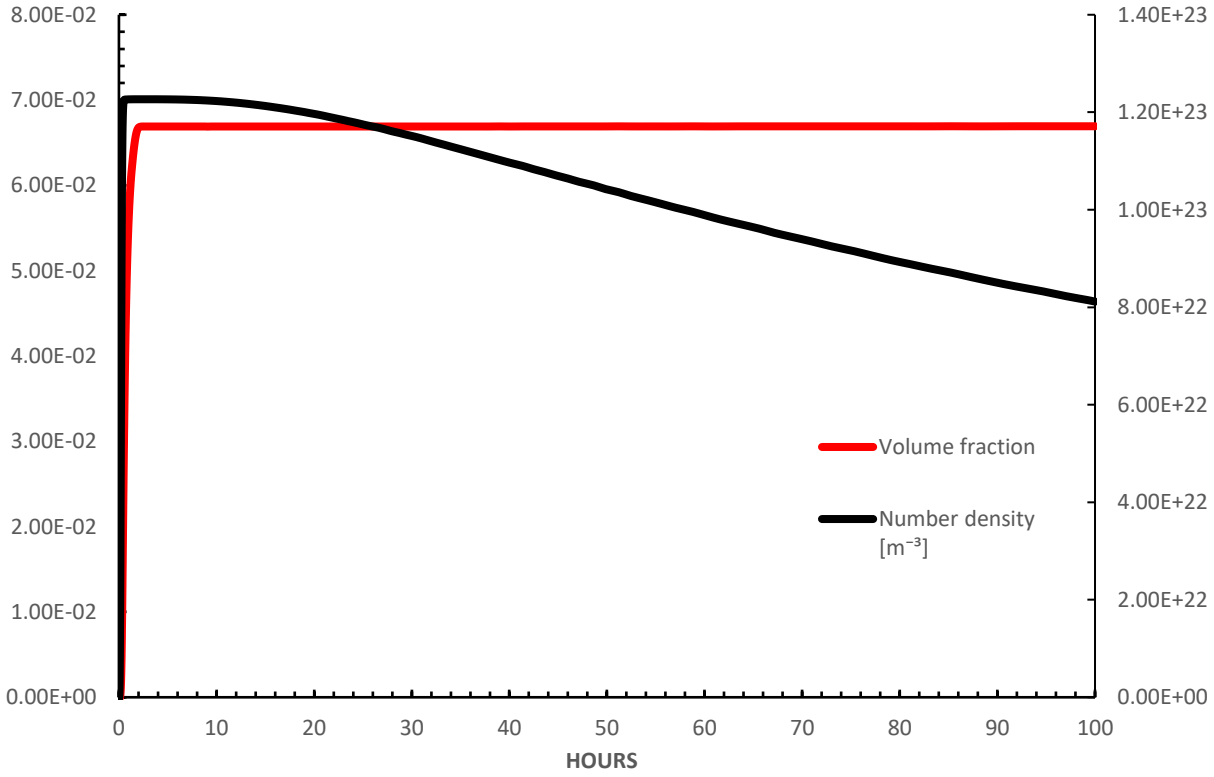

Figure 4-29: Evolution of number density and volume fraction in the aging process of 170°C, in the Al-4.35Cu-1.5Mg alloy with a mobility prefactor of 0.2.

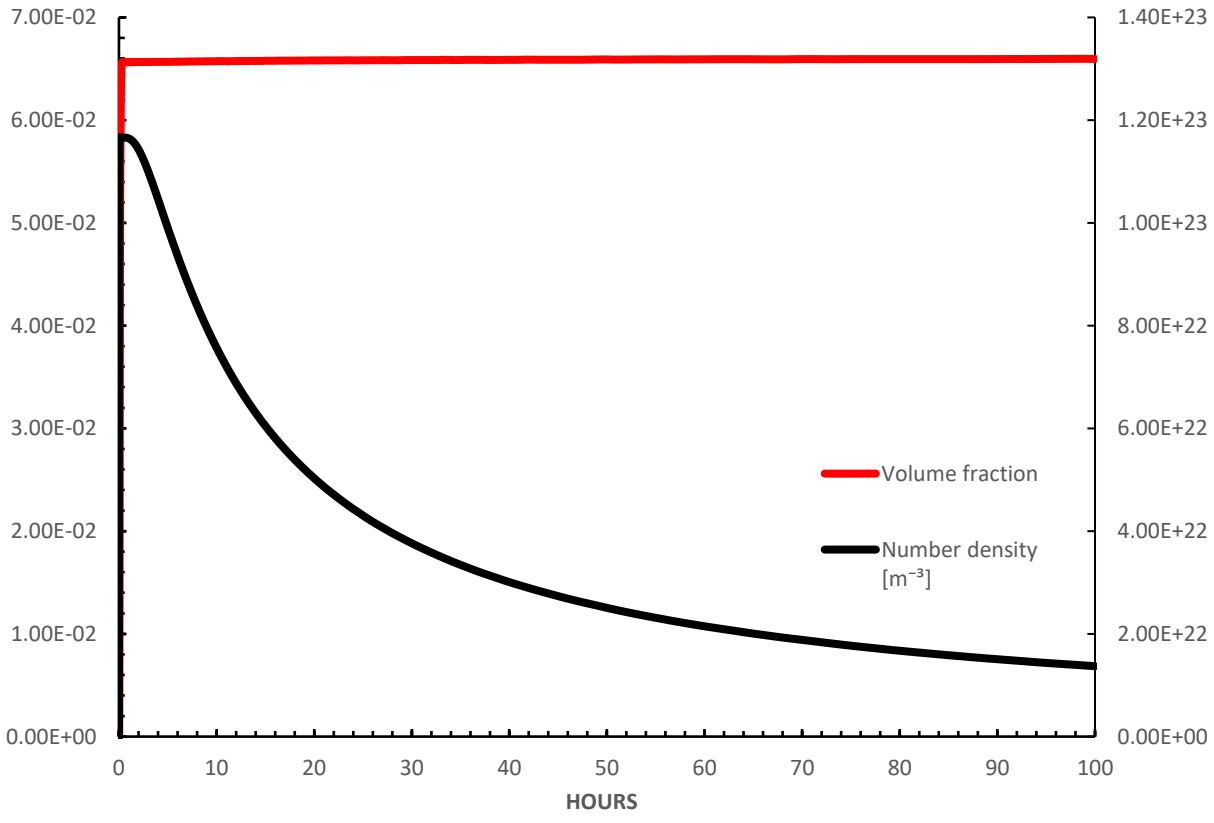

Figure 4-30: Evolution of number density and volume fraction in the aging process of 210°C, in the Al-4.35Cu-1.5Mg alloy with a mobility prefactor of 0.1.

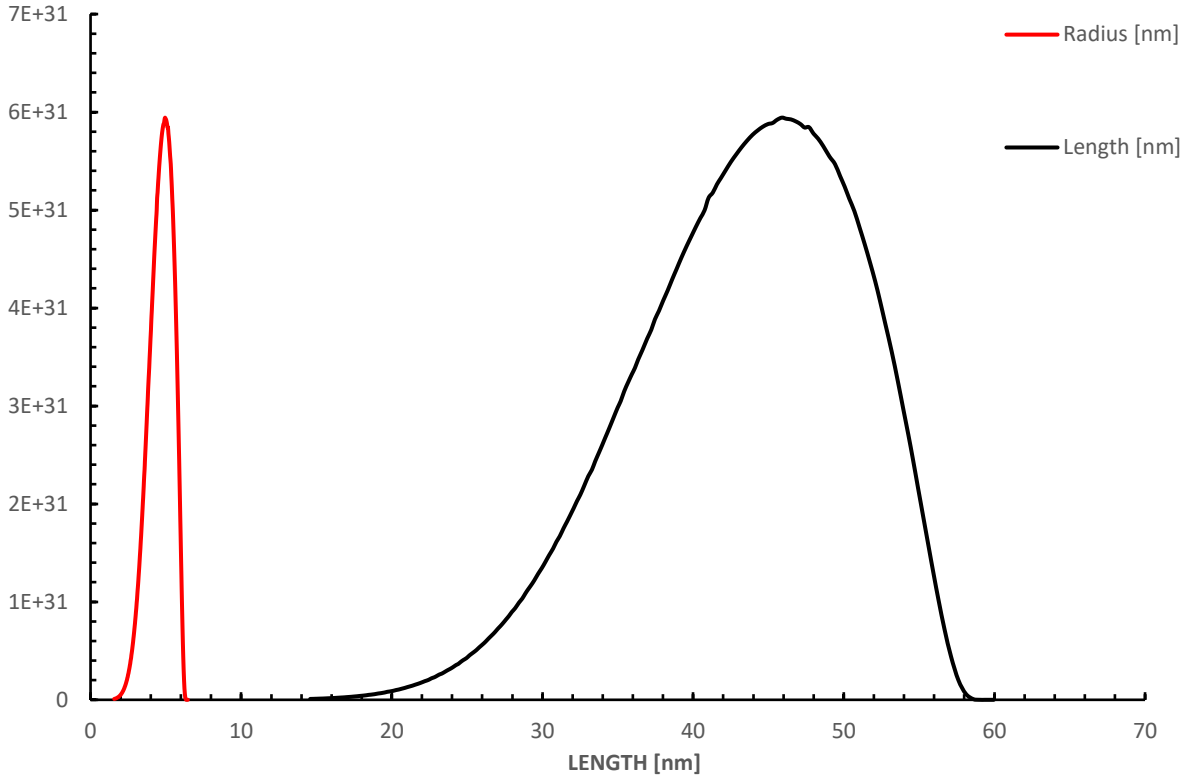

Figure 4-31: Radius and length size distributions of the S phase precipitates, at peak hardness in 170°C , for the Al-4.35Cu-1.5Mg alloy with needle-shaped precipitates (A.R:10) and a mobility prefactor of 0.2.

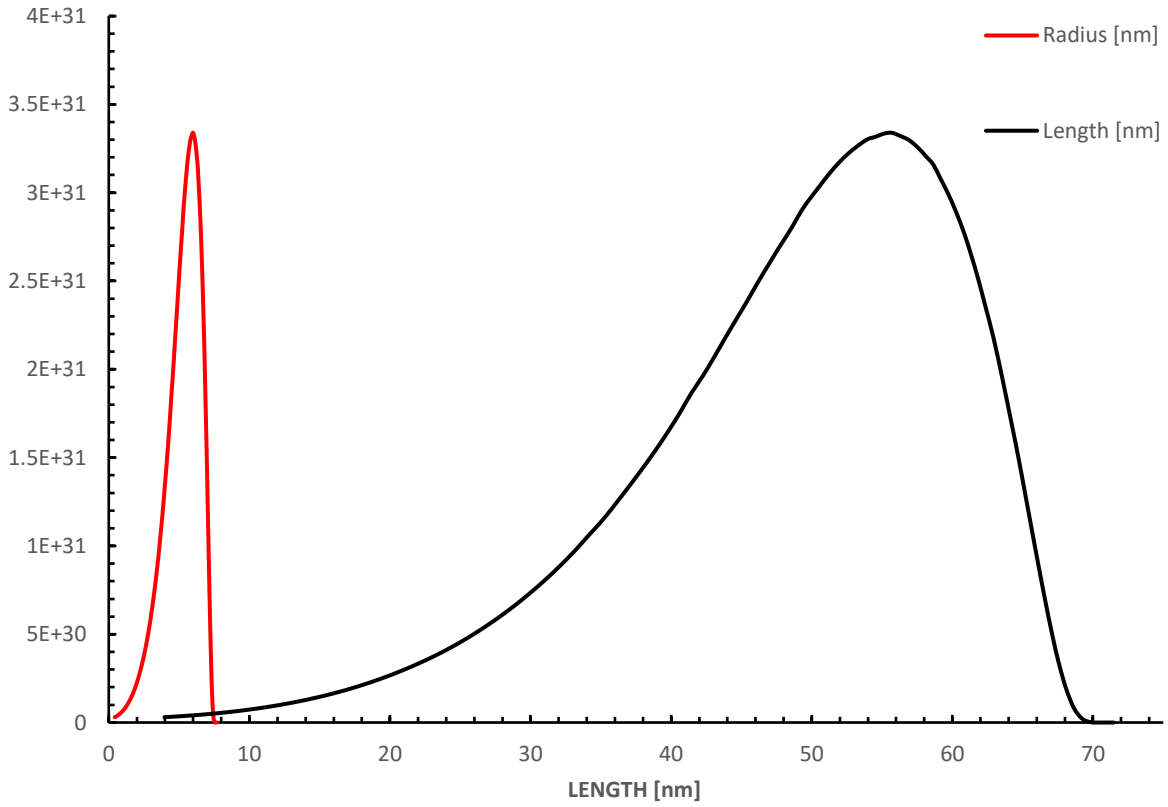

Figure 4-32: Radius and length size distributions of the S phase precipitates, at peak hardness in 210°C , for the Al-4.35Cu-1.5Mg alloy with needle-shaped precipitates (A.R:10) and a mobility prefactor of 0.1.

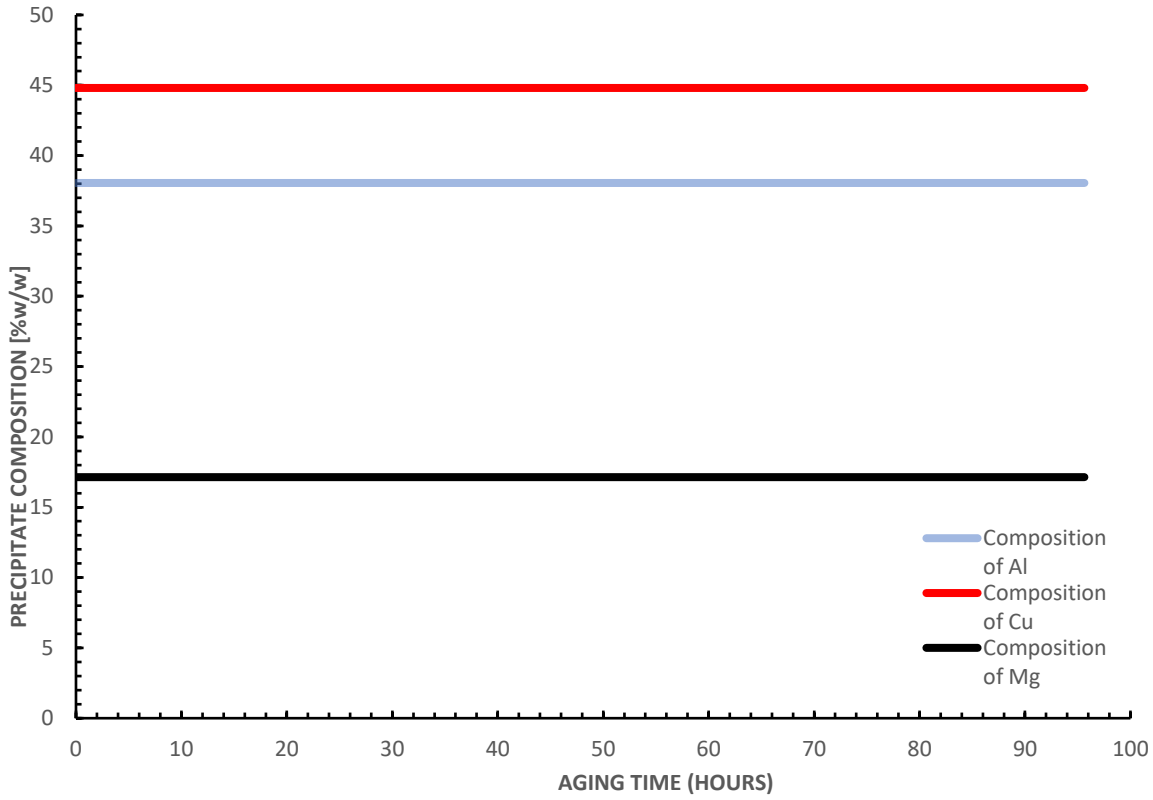

Figure 4-33: Precipitate Composition (% w/w) during aging for both 170°C and 210°C, for the Al-4.35Cu-1.5Mg alloy with needle-shaped precipitates (A.R:10) and a mobility prefactor 0.2 and 0.1, respectively.

Chapter 5 Conclusions

The microstructural changes occurring in the aging precipitation of the aluminum alloy 2024 were examined using microhardness measurements, and modeling by utilizing the TC-PRISMA precipitation model. The findings of this investigation could provide valuable insights for the design of aging treatments and their applications, as well as for future studies related to the behavior of heat-treatable aluminum alloys during the precipitation process.

The outcomes from the microhardness measurements conducted on three distinct aging heat treatments revealed noteworthy findings regarding the aluminum alloy AA2024. When subjected to an aging process at 150°C and 160°C, the alloy exhibited a favorable response when it was subjected to a modified mobility prefactor. In the first case, a prefactor of 0.2 was selected achieving a peak hardness of 154HV within a reasonable duration of 96-120 hours while in the second case of 160°C, a mobility prefactor of 0.1 achieved great accuracy with the peak hardness of 157HV being reached at the same time as the experiment. When it comes to the temperature of 170°C, the model results were compared to different experiments that were conducted by Floratos and Karantonidis, with different experimental measurements. The model reached a great accuracy with a mobility prefactor of 0.1 for the former, with a peak hardness of 129HV in 48 hours, while, for the latter, the prefactor was not modified as great accuracy was achieved from the beginning, reaching a peak hardness of 129HV in 6 hours, the same as the experiment. For 210°C, peak hardness, in both the experiment and the model, was achieved in 1 hour and a value of 125HV was reached in both scenarios. The mobility prefactor in this case was modified by 0.3.

In every case, the peak hardness was achieved with near-perfect precision, and only minor discrepancies were noted in the rates of both hardness increase and decrease. Additionally, there was an attempt to assume two main hardening phases of S and S’ phase but there was no available interfacial energy in the bibliography for the latter. When taken individually, with every setting at default in TC-PRISMA except the needle morphology, the model resulted in exactly the same hardness curve, confirming the argument made from other researchers that the S’ and S phase are identical. From that point, the was an attempt to modify the model by assuming needle-shaped precipitates with an aspect ratio of 10, for the temperatures of 170°C and 210°C. When compared to the sphered shaped precipitates, peak hardness was not affected but the time to reach it was, requiring even smaller prefactors to achieve the same results. There was, also, an attempt to extract some important information for other characteristic quantities such as the nucleation rate, the normalized driving force, the number density, the volume fraction of the S phase, size distributions and, finally, the composition of the precipitates. In 170°C, the volume fraction of S phase reached 0.067 at peak hardness and a predominant majority of the precipitates exhibited a radius of approximately 4.94nm and a length of approximately 45.9nm. In 210°C, the volume fraction of S phase reached 0.06566 at peak hardness and a predominant majority of the precipitates exhibited a radius of approximately 6nm and a length of approximately 55.67nm. The chemical composition, in both temperatures, was found to be identical and was calculated as (38.05)Al(17.14)Mg(44.81)Cu.

Additional research is necessary to attain more precise values for the parameters associated with the precipitation model. This extended inquiry could encompass the following avenues of investigation:

- Utilizing advanced electronic microscopes (such as SEM, TEM, HREM) for metallography, enabling the observation and identification of minute particles (e.g., hardening precipitates or dispersoids) as well as the determination of their key attributes (including structure, size, chemical composition, and morphology).

- Employing the Differential Scanning Calorimetry (DSC) technique to characterize the reactions that take place during the dissolution or formation of precipitates. This would involve interpreting thermograms for various aging stages of the material to gain insights into the underlying processes.

Chapter 6 References

[1] F. Zhang, L.E. Levine, A.J. Allen, C.E. Campbell, A.A. Creuziger, N. Kazantseva, J. Ilavsky, In situ structural characterization of ageing kinetics in aluminum alloy 2024 across angstrom-to-micrometer length scales, Acta Mater. 111 (2016) 385–398. https://doi.org/10.1016/j.actamat.2016.03.058.

[2] S.C. Wang, M.J. Starink, Two types of S phase precipitates in Al–Cu–Mg alloys, Acta Mater. 55 (2007) 933–941. https://doi.org/10.1016/j.actamat.2006.09.015.

[3] G. Sha, R.K.W. Marceau, X. Gao, B.C. Muddle, S.P. Ringer, Nanostructure of aluminium alloy 2024: Segregation, clustering and precipitation processes, Acta Mater. 59 (2011) 1659–1670. https://doi.org/10.1016/j.actamat.2010.11.033.

[4] C. Pan, Y. Yang, S. Wang, Y. Liu, S. Hu, Z. Wang, P. Shen, Atomistic building blocks of one-dimensional Guinier–Preston–Bagaryatsky zones in Al-Cu-Mg alloys, Mater. Des. 187 (2020) 108393. https://doi.org/10.1016/j.matdes.2019.108393.

[5] N. Radutoiu, J. Alexis, L. Lacroix, M. Abrudeanu, J. Petit, Study of the Influence of the Artificial Ageing Temperature on the AA2024 Alloy Microstructure, Key Eng. Mater. 550 (2013) 115–125. https://doi.org/10.4028/www.scientific.net/KEM.550.115.

[6] V.A. Esin, L. Briez, M. Sennour, A. Köster, E. Gratiot, J. Crépin, Precipitation-hardness map for Al–Cu–Mg alloy (AA2024-T3), J. Alloys Compd. 854 (2021) 157164. https://doi.org/10.1016/j.jallcom.2020.157164.

[7] C. Zhu, K. Lv, B. Chen, On the S-phase precipitates in 2024 aluminum alloy: An atomic-scale investigation using high-angle annular dark-field scanning transmission electron microscopy, J. Mater. Res. 35 (2020) 1–8. https://doi.org/10.1557/jmr.2020.74.

[8] Y. Jialin, Strength Modelling of Al-Cu-Mg Type Alloys, (n.d.).

[9] G.N. Haidemenopoulos, Physical Metallurgy: Principles and Design, CRC Press, Boca Raton, 2018. https://doi.org/10.1201/9781315211220.

[10] Aluminium alloys for aircraft structures, in: Introd. Aerosp. Mater., Elsevier, 2012: pp. 173–201. https://doi.org/10.1533/9780857095152.173.

[11] Principles of Heat Treating of Nonferrous Alloys, (2016). https://doi.org/10.31399/asm.hb.v04e.a0006250.

[12] R.P. Garrett, J. Lin, T.A. Dean, An investigation of the effects of solution heat treatment on mechanical properties for AA 6xxx alloys: experimentation and modelling, Int. J. Plast. 21 (2005) 1640–1657. https://doi.org/10.1016/j.ijplas.2004.11.002.

[13] D.A.P. Sherif Kenneth E. Easterling, Mohamed Y., Phase Transformations in Metals and Alloys, 4th ed., CRC Press, Boca Raton, 2021. https://doi.org/10.1201/9781003011804.

[14] R.E. Smallman, A.H.W. Ngan, Chapter 7 - Mechanical properties II — Strengthening and toughening, in: R.E. Smallman, A.H.W. Ngan (Eds.), Phys. Metall. Adv. Mater. Eng. Seventh Ed., Butterworth-Heinemann, Oxford, 2007: pp. 385–446. https://doi.org/10.1016/B978-075066906-1/50010-X.

[15] J. Lendvai, The effect of vacancy-rich clusters on the decomposition processes in Al-Zn-Mg alloys, Cryst. Res. Technol. 19 (1984) 1341–1346. https://doi.org/10.1002/crat.2170191017.

[16] Reaction kinetics in processes of nucleation and growth | BibSonomy, (n.d.). https://www.bibsonomy.org/bibtex/e3bf174ae0d30d926bcb85c2c5bc410f (accessed May 16, 2023).

[17] M. Avrami, Kinetics of Phase Change. I General Theory, J. Chem. Phys. 7 (2004) 1103–1112. https://doi.org/10.1063/1.1750380.

[18] The Theory of Transformations in Metals and Alloys - 1st Edition, (n.d.). https://shop.elsevier.com/books/the-theory-of-transformations-in-metals-and-alloys/christian/978-0-08-044019-4 (accessed July 14, 2023).

[19] M. Perez, Gibbs–Thomson effects in phase transformations, Scr. Mater. 52 (2005) 709–712. https://doi.org/10.1016/j.scriptamat.2004.12.026.

[20] G.W. Greenwood, The growth of dispersed precipitates in solutions, Acta Metall. 4 (1956) 243–248. https://doi.org/10.1016/0001-6160(56)90060-8.
[21] I.M. Lifshitz, V.V. Slyozov, The kinetics of precipitation from supersaturated solid solutions, J. Phys. Chem. Solids. 19 (1961) 35–50. https://doi.org/10.1016/0022-3697(61)90054-3.
[22] C. Wagner, Theorie der Alterung von Niederschlägen durch Umlösen (Ostwald-Reifung), Z. Für Elektrochem. Berichte Bunsenges. Für Phys. Chem. 65 (1961) 581–591. https://doi.org/10.1002/bbpc.19610650704.
[23] J.L. García-Hernández, C.G. Garay-Reyes, I.K. Gómez-Barraza, M.A. Ruiz-Esparza-Rodríguez, E.J. Gutiérrez-Castañeda, I. Estrada-Guel, M.C. Maldonado-Orozco, R. Martínez-Sánchez, Influence of plastic deformation and Cu/Mg ratio on the strengthening mechanisms and precipitation behavior of AA2024 aluminum alloys, J. Mater. Res. Technol. 8 (2019) 5471–5475. https://doi.org/10.1016/j.jmrt.2019.09.015.
[24] Y.C. Lin, Y.-C. Xia, Y.-Q. Jiang, H.-M. Zhou, L.-T. Li, Precipitation hardening of 2024-T3 aluminum alloy during creep aging, Mater. Sci. Eng. A. 565 (2013) 420–429. https://doi.org/10.1016/j.msea.2012.12.058.
[25] I.N. Khan, M.J. Starink, J.L. Yan, A model for precipitation kinetics and strengthening in Al–Cu–Mg alloys, Mater. Sci. Eng. A. 472 (2008) 66–74. https://doi.org/10.1016/j.msea.2007.03.033.
[26] S.C. Wang, M.J. Starink, N. Gao, Precipitation hardening in Al–Cu–Mg alloys revisited, Scr. Mater. 54 (2006) 287–291. https://doi.org/10.1016/j.scriptamat.2005.09.010.
[27] M.J. Starink, N. Gao, J.L. Yan, The origins of room temperature hardening of Al–Cu–Mg alloys, Mater. Sci. Eng. A. 387–389 (2004) 222–226. https://doi.org/10.1016/j.msea.2004.01.085.
[28] M.J. Starink, S.C. Wang, The thermodynamics of and strengthening due to co-clusters: General theory and application to the case of Al–Cu–Mg alloys, Acta Mater. 57 (2009) 2376–2389. https://doi.org/10.1016/j.actamat.2009.01.021.
[29] Y. Chen, N. Gao, G. Sha, S. Ringer, M. Starink, Microstructural evolution, strengthening and thermal stability of an ultrafine-grained Al–Cu–Mg alloy, Acta Mater. 109 (2016) 202–212. https://doi.org/10.1016/j.actamat.2016.02.050.
[30] S.P. Ringer, K. Hono, T. Sakurai, I.J. Polmear, Cluster hardening in an aged Al-Cu-Mg alloy, Scr. Mater. 36 (1997) 517–521. https://doi.org/10.1016/S1359-6462(96)00415-0.
[31] A. Ardell, Precipitation Hardening, Metall. Trans. A. 16 (1985) 2131–2165. https://doi.org/10.1007/BF02670416.
[32] B. Reppich, Particle Strengthening, in: Mater. Sci. Technol., John Wiley & Sons, Ltd, 2006. https://doi.org/10.1002/9783527603978.mst0054.
[33] M. Starink, N. Gao, L. Davin, J.L. Yan, A. Cerezo, Room temperature precipitation in quenched Al-Cu-Mg alloys: A model for the reaction kinetics and yield strength development, Philos. Mag. 85 (2005) 1395–1417. https://doi.org/10.1080/14786430412331333374.
[34] X. Chen, C.D. Marioara, S.J. Andersen, J. Friis, A. Lervik, R. Holmestad, E. Kobayashi, Precipitation processes and structural evolutions of various GPB zones and two types of S phases in a cold-rolled Al-Mg-Cu alloy, Mater. Des. 199 (2021) 109425. https://doi.org/10.1016/j.matdes.2020.109425.
[35] S. Abis, M. Massazza, P. Mengucci, G. Riontino, Early ageing mechanisms in a high-copper AlCuMg alloy, Scr. Mater. 45 (2001) 685–691. https://doi.org/10.1016/S1359-6462(01)01080-6.
[36] Y.A. Bagaryatsky, Structural changes on aging Al-Cu-Mg alloys, in: Dokl Akad SSSR, 1952: pp. 397–559.
[37] Z.R. Liu, J.H. Chen, S.B. Wang, D.W. Yuan, M.J. Yin, C.L. Wu, The structure and the properties of S-phase in AlCuMg alloys, Acta Mater. 59 (2011) 7396–7405. https://doi.org/10.1016/j.actamat.2011.08.009.
[38] N.D. Alexopoulos, Z. Velonaki, C.I. Stergiou, S.K. Kourkoulis, Effect of ageing on precipitation kinetics, tensile and work hardening behavior of Al-Cu-Mg (2024) alloy, Mater. Sci. Eng. A. 700 (2017) 457–467. https://doi.org/10.1016/j.msea.2017.05.090.
[39] J.M. Silcock, THE STRUCTURAL AGEING CHARACTERISTICS OF ALUMINIUM-COPPER-LITHIUM ALLOYS, J Inst Met. Vol: 88 (1960). https://www.osti.gov/biblio/4138237 (accessed May 25, 2023).

[40] Zahra Am, Zahra Cy, C. Alfonso, A. Chara, Comments on ꜀luster hardening in an aged Al-Cu-Mg alloy - Structure and Properties, (n.d.). https://elibrary.ru/item.asp?id=86586 (accessed May 25, 2023).
[41] P. Ratchev, B. Verlinden, P. De Smet, P. Van Houtte, Precipitation hardening of anAl–4.2wt% Mg–0.6wt% Cu alloy, Acta Mater. 46 (1998) 3523–3533. https://doi.org/10.1016/S1359-6454(98)00033-0.
[42] H.C. Shih, N.-J. Ho, J. Huang, Precipitation behaviors in Al-Cu-Mg and 2024 aluminum alloys, Metall. Mater. Trans. A. 27 (1996) 2479–2494. https://doi.org/10.1007/BF02652342.
[43] N. Gao, L. Davin, S.P. Wang, A. Cerezo, M.J. Starink, Precipitation in Stretched Al-Cu-Mg Alloys with Reduced Alloying Content Studied by DSC, TEM and Atom Probe, Mater. Sci. Forum. 396–402 (2002) 923–928. https://doi.org/10.4028/www.scientific.net/MSF.396-402.923.
[44] M. Starink, I. Sinclair, N. Gao, N. Kamp, P. Gregson, P. Pitcher, A. Levers, S. Gardiner, Development of New Damage Tolerant Alloys for Age-Forming, Mater. Sci. Forum - MATER SCI FORUM. 396–402 (2002) 601–606. https://doi.org/10.4028/www.scientific.net/MSF.396-402.601.
[45] A. Charai, T. Walther, C. Alfonso, A.-M. Zahra, C.Y. Zahra, Coexistence of clusters, GPB zones, S''-, S'- and S-phases in an Al–0.9% Cu–1.4% Mg alloy, Acta Mater. 48 (2000) 2751–2764. https://doi.org/10.1016/S1359-6454(99)00422-X.
[46] V. Radmilovic, G. Thomas, G.J. Shiflet, E.A. Starke, On the nucleation and growth of Al2CuMg (S') in Al□Li□Cu□Mg and Al□Cu□Mg alloys, Scr. Metall. 23 (1989) 1141–1146. https://doi.org/10.1016/0036-9748(89)90315-3.
[47] S.P. Ringer, T. Sakurai, I.J. Polmear, Origins of hardening in aged Al□Gu□Mg□(Ag) alloys, Acta Mater. 45 (1997) 3731–3744. https://doi.org/10.1016/S1359-6454(97)00039-6.
[48] S.P. Ringer, K. Hono, Microstructural Evolution and Age Hardening in Aluminium Alloys: Atom Probe Field-Ion Microscopy and Transmission Electron Microscopy Studies, Mater. Charact. 44 (2000) 101–131. https://doi.org/10.1016/S1044-5803(99)00051-0.
[49] S.P. Ringer, K. Hono, I.J. Polmear, T. Sakurai, Nucleation of precipitates in aged AlCuMg(Ag) alloys with high Cu:Mg ratios, Acta Mater. 44 (1996) 1883–1898. https://doi.org/10.1016/1359-6454(95)00314-2.
[50] L. Reich, S.P. Ringer, K. Hono, Origin of the initial rapid age hardening in an Al-1.7 at.% Mg-1.1 at.% Cu alloy, Philos. Mag. Lett. 79 (1999) 639–648. https://doi.org/10.1080/095008399176689.
[51] S.P. Ringer, S.K. Caraher, I.J. Polmear, Response to comments on cluster hardening in an aged Al-Cu-Mg alloy, Scr. Mater. 39 (1998) 1559–1567. https://doi.org/10.1016/S1359-6462(98)00364-9.
[52] L. Kovarik, P.I. Gouma, C. Kisielowski, S.A. Court, M.J. Mills, A HRTEM study of metastable phase formation in Al–Mg–Cu alloys during artificial aging, Acta Mater. 52 (2004) 2509–2520. https://doi.org/10.1016/j.actamat.2004.01.041.
[53] S.C. Wang, M.J. Starink, The assessment of GPB2/S'' structures in Al–Cu–Mg alloys, Mater. Sci. Eng. A. 386 (2004) 156–163. https://doi.org/10.1016/j.msea.2004.07.006.
[54] S.C. Wang, M.J. Starink, Precipitates and intermetallic phases in precipitation hardening Al–Cu–Mg–(Li) based alloys, Int. Mater. Rev. 50 (2005) 193–215. https://doi.org/10.1179/174328005X14357.
[55] R.N. Wilson, D.M. Moore, P.J.E. Forsyth, Effects of 0.25% silicon on precipitation processes in an aluminium -2.5% copper -1.2% magnesium alloy, RAE Tech. Rep. No 66063. (1966). https://repository.tudelft.nl/islandora/object/uuid%3Abf6d85b5-d04b-4f13-8b00-2e26495139e0 (accessed July 15, 2023).
[56] Α.-Μ.Χ. Κεφαλάς, Corrosion-induced hydrogen absorption and the effect of aging treatment in Aluminum alloy 2024, bachelorThesis, 2020. http://ir.lib.uth.gr/xmlui/handle/11615/52147 (accessed June 9, 2023).
[57] Π. Φλωράτος, Effect of aging time on corrosion-induced hydrogen trapping in high-strength Al-Alloy 2024, bachelorThesis, 2016. http://ir.lib.uth.gr/xmlui/handle/11615/48091 (accessed June 9, 2023).

[58] Χ.Θ. Καραντωνίδης, Effect of aging on corrosion-induced hydogen trapping of aluminum alloy 2024, bachelorThesis, 2017. http://ir.lib.uth.gr/xmlui/handle/11615/47163 (accessed June 9, 2023).
[59] J.E. Morral, G.R. Purdy, Particle coarsening in binary and multicomponent alloys, Scr. Metall. Mater. 30 (1994) 905–908. https://doi.org/10.1016/0956-716X(94)90413-8.
[60] J.S. Langer, A.J. Schwartz, Kinetics of nucleation in near-critical fluids, Phys. Rev. A. 21 (1980) 948–958. https://doi.org/10.1103/PhysRevA.21.948.